Signal feedback applications in low-field NMR and MRI

Vyacheslav V Kuzmin, Pierre-Jean Nacher

To cite this version:

Vyacheslav V Kuzmin, Pierre-Jean Nacher. Signal feedback applications in low-field NMR and MRI. 2019. hal-02069159v1

HAL Id: hal-02069159
https://hal.science/hal-02069159v1

Preprint submitted on 12 Jul 2019 (v1), last revised 17 Sep 2019 (v2)

HAL is a multi-disciplinary open access archive for the deposit and dissemination of scientific research documents, whether they are published or not. The documents may come from teaching and research institutions in France or abroad, or from public or private research centers.

L'archive ouverte pluridisciplinaire **HAL**, est destinée au dépôt et à la diffusion de documents scientifiques de niveau recherche, publiés ou non, émanant des établissements d'enseignement et de recherche français ou étrangers, des laboratoires publics ou privés.

Signal feedback applications in low-field NMR and MRI

Vyacheslav V. Kuzmin*[1,2] and Pierre-Jean Nacher†[1]

[1] *Laboratoire Kastler Brossel, ENS-Université PSL, CNRS, Sorbonne Université, Collège de France; 24 rue Lhomond, 75005 Paris, France.*

[2] *Present address: Institute of Physics, Kazan Federal University, Kremlevskaya 18, 420008 Kazan, Russia.*

Abstract Tuned pick-up coils with high quality factors Q are used in NMR and MRI for high-sensitivity and low-noise detection. However, large Q-factors introduce bandwidth issues at low frequency and the associated enhanced currents may cause significant radiation damping effects, especially with hyperpolarised samples. Signal feedback can be used to actively control these currents and adjust the detection bandwidth without resistive losses. Capacitive and inductive coupling methods are compared using detailed models and the operating conditions for efficient feedback with negligible noise penalty are discussed. Several high-impedance commercial preamplifiers have been found to affect the resonance characteristics of tuned coils in a gain-dependent way, or could not be used in low-frequency NMR because of oscillations at large positive gain. This is attributed to an undocumented internal feedback, and could be neutralised using external feedback. The implementation of an inductive coupling scheme to feed a suitably amplified phase-adjusted signal back into the PU coils of low-field NMR systems is described, and three experimental applications are reported. One system is used for NMR studies of distant dipolar field effects in highly polarized liquid ^{3}He without or with radiation damping. The moderate intrinsic Q-factor ($\approx$7) could be reduced (down to 1) or increased (up to 100) to control transient maser oscillations. Another system was used for MRI of water samples around 2 mT with Q $\approx$190 Litz-wire detection coils. The detection bandwidth was increased by actively reducing the Q-factor to obtain uniform sensitivities in images and avoid artifacts introduced by intensity corrections. Finally, parallel acquisition in MRI was performed using two separately tuned detection coils placed above and below the sample. They were actively decoupled using two feedback systems. For an imaging field of view smaller than the sample, artifact-free unfolded images demonstrate the efficiency of this active coil decoupling scheme.

Keywords: Low-field NMR; low-field MRI; signal feedback; radiation damping; quality factor; Q-factor

1 Introduction

High quality pick-up (PU) coils, usually tuned with capacitors, are commonly used in nuclear magnetic resonance and magnetic resonance imaging (NMR and MRI) for highly sensitive detection. Because the signal-to-noise ratio (SNR) scales with the quality factor Q of the tuned coil as $\sqrt{Q}$ [1, 2] it is important to have as high a Q-factor as possible. This is crucial at low NMR frequencies when losses attributed to the resistance of the coil wires are dominant compared to the unavoidable losses in conductive samples [3, 4, 5] and therefore govern the achievable SNR. In that sense, low-frequency typically means up to 1 MHz for whole-body MRI, but this value depends on conductivity and dimensions of the sample as well as on configuration, temperature and dimensions of the coil [6, 7]. However, using a high-Q tuned coil (a tank circuit) for NMR detection can induce the well-known and usually adverse effects of radiation damping (RD) [8, 9], as well as long ring-down times after radiofrequency (RF) pulses and bandwidth issues in low field MRI (where the required bandwidth can be larger than that of the tank circuit). RD is caused by the reaction RF field generated by the current in the PU coil that is driven by NMR precession. RD can strongly affect lifetimes of NMR signals. RD can also modify NMR precession frequencies if the reaction field (its co-rotating term) is not perfectly out-of-phase with respect to the transverse magnetisation: this is the so-called frequency pushing or cavity pulling effect [10, 11]. The issues raised by using a high-Q tuned coil in detection become more significant if hyperpolarisation methods are exploited for enhanced NMR sensitivity due to the correspondingly increased RD role.

The easiest way to overcome the drawbacks arising from narrow bandwidths or strong RD consists in passively spoiling the Q-factor by adding, for instance, a resistor across the tank circuit. Of course, this is unsuitable for highly sensitive (high-SNR) detection.

Electronic feedback (abbreviated to FB in the following) is widely used to tailor the input impedance of a preamplifier (PA in the following) and may therefore modify the Q-factor of a detection circuit. When negative FB is applied, this can be imagined as adding a noiseless resistor in parallel with the input of the front-end signal PA. It loads the detection tank circuit and therefore broadens the detection bandwidth and reduces RD without noise penalty (by active Q-damping). The fact that negative FB can reduce currents in detection coils (and therefore magnetic coupling between neighbouring coils) can be exploited for efficient RF coil array decoupling in parallel

---

*slava625@yandex.ru.

†nacher@lkb.ens.fr, corresponding author.

imaging [12]. This is similar to the high frequency approach in which high impedance PAs with appropriate passive impedance matching networks are used for this purpose [13]. Conversely, positive FB can be used to artificially increase RD, e.g. for magnetometry applications when a self-sustained NMR signal (maser operation) is needed [14].

The possible use of negative FB to damp Q-factors in NMR detection was first considered from a theoretical point of view in 1959 by Chidambaram [15]. At the same time, Szoke and Meiboom [16] used positive FB within a PA to increase Q-factors in a study of RD and NMR masers, but they did not provide any details. Hoult was first to describe and implement negative FB for improved NMR detection by means of capacitive coupling within the front-end PA [17].

Two families of FB schemes can be distinguished. The first one includes schemes which indirectly modify the reaction RF field (RD field) through a modification of the detection circuit (more precisely, through a modification of its effective Q-factor). This means that this FB approach modifies the response of the detection to any external signal generated in the PU coil; all the abovementioned FB schemes belong to this family. An example of such a scheme at high frequencies is the "Brussels"scheme [9] which uses inductive coupling for generating a suitably amplified FB electromotive force (emf) in the coil, in such a way that it tends to oppose the emf induced by precessing magnetisation. It can be used with minor modifications at low frequencies as well [18]. The second family includes FB schemes involving a direct action on magnetisation by generating an additional RF reaction field without affecting detection. The signal resulting from an emf induced in the PU coil is thus unchanged when this type of FB is applied. The "Ecole Polytechnique"scheme [19] is an example of such a scheme at high frequencies. It uses a directional coupler to feed back a suitably amplified current in the NMR resonator, hence this does not affect the signal at the PA output. This type of FB scheme can be used for controlling RD without raising the delicate issue of detection stability, but it is not suitable for broadband detection and fast ring-down in low frequency NMR. In the remainder of this article, we will thus only consider schemes belonging to the first family.

The purpose of this article is to demonstrate the efficiency of signal FB in NMR detection for a range of low field applications whenever RD and detection bandwidth need to be under control. We consider two different FB implementations: in the first one, FB current is injected directly into the detection tank circuit. This is similar to the method described in Ref. [17] and we refer to it as capacitive FB for convenience (it was initially used with capacitive coupling within the PA). The second implementation relies on a transformer or weak inductive coupling to generate a FB emf in the tank circuit. This is similar to the "Brussels" scheme [9] and we simply call it inductive FB. Although we experimentally used the second implementation, with inductive coupling between the PA output and the PU coil, most of the effects of FB will be described in terms of changes of the input impedance of the PA. This is quite similar to the capacitive FB scheme described in Ref. [17], but the RD field cannot be directly computed using this approach.

The structure of this article is the following: In Sec. 2.1 we describe a typical low frequency NMR Faraday detection system including a tuned coil and a PA, and introduce SNR optimisation issues. The so-called noise matching of a tuned PU coil with a PA for broadband detection at low frequency is discussed. Sec. 2.2 describes the main features of two kinds of FB models and simplified results obtained in a high-gain limit (full derivations are given in App. B). In Sec. 3 we first report and discuss experimental evidence of significant internal FB in PAs (Sec. 3.1). It was revealed by the observation of gain-dependent effective quality factors of tank circuits connected to the inputs of these PAs, an effect which was noticed for probes in high-field NMR spectrometers as well [20], and was consistently observed for several high-impedance commercial PAs. We then describe the actual implementation of inductive FB (Sec. 3.2) and report on its use to control RD (Sec. 3.3), to increase detection bandwidth in MRI (Sec. 3.4) and to perform parallel acquisition in MRI (Sec. 3.5).

2 Theory and models

2.1 Faraday detection at low frequencies

NMR signals are usually obtained during free precession via Faraday induction in a coil surrounding the sample. This PU coil is typically tuned with a capacitor to the Larmor precession frequency and is connected to a PA serving to boost the signal level for proper recording (see Fig. 1, where the PU coil consists of two rectangular-shaped windings connected in series). The choice of PU coil shape and size depends on experimental constraints, such as the available space for the sample and the coil. A solenoid coil is the best solution in terms of SNR because of its highest filling factor [1], but saddle-shaped coils or Helmholtz-like pairs of coils are also often used in NMR and MRI at low frequencies. The resistance of the coil and the input stage of the PA independently add broadband noise to the NMR signal. In this article we do not discuss the choice of coil geometry, but only address the issue of finding the optimal coil winding parameters to achieve the best SNR, either at the central frequency of the tank circuit or over any desired frequency range, for given coil shape and dimensions, and PA specifications.

The notations for voltages and currents in AC circuit analyses correspond to the following conventions: time-dependent (complex) voltage and current signals and noises are indicated by lower case letters (e_S, i_S, etc.). The corresponding root mean square (rms) voltages and

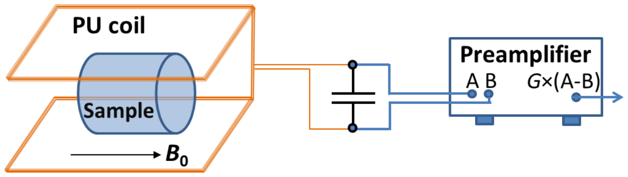

Figure 1: Sketch of a Faraday detection scheme for low-frequency NMR or MRI. The receive-only PU wire-wound coil may comprise many turns of enamelled copper or litz wire. The high-impedance tuned tank circuit is directly connected to the high impedance input of the PA, usually without any impedance transformation network. Here, differential amplification is sketched, but most PAs have a single-ended input (see App. A). The usual 50 Ω power-matching condition of high-frequency RF electronics is replaced with a noise-matching condition to the PA input (Sec. 2.1.2). No additional electronics (Q-switch, signal FB system) is displayed and the crossed transmit coil is not shown for simplicity.

currents over a specified bandwidth Δf are indicated by upper case letters ($E_{\rm S}$, $I_{\rm S}$, etc). We generically use the letter Z for complex impedances and Y for complex admittances. Impedances and admittances with identical subscripts (and sometimes superscripts) correspond to reciprocal quantities, e.g., $Y_C = 1/Z_C$.

2.1.1 The pick-up coil

We consider here the case of a low enough NMR frequency f for which the detection circuit consists of lumped elements, the PU coil and the tuning capacitor. Moreover, f is assumed to be much lower than the self-resonance frequency of the PU coil, a condition for maintaining a constant phase of the induced emf in all parts of the coil [21, 22] (the self-resonance is due to stray capacitance between adjacent loops and layers in the coil and therefore depends on the coil details). Under such conditions the emf $E_{\rm coil}$ produced in a coil of given dimensions by the precessing magnetisation of a sample is proportional to the number of turns, N. We further assume that the sample noise due to the sample electrical conductivity [3, 4] is negligible compared to the Johnson noise in the coil, i.e. that $R_{\rm S} \ll R_{\rm coil}$, where $R_{\rm S}$ is the sample equivalent resistance and $R_{\rm coil}$ is the coil series AC resistance. This is normally the case for low frequencies or small samples [5, 6, 7]. As a rule of thumb, this is true for in-vivo NMR with room-temperature copper coils provided that $fa^2 < 100$ MHz cm^2 [2], where a is the typical radius of the coil and sample. The rms Johnson noise over a bandwidth Δf is $E^{\rm n}_{\rm coil} = \sqrt{4k_{\rm B}T_{\rm coil}R_{\rm coil}\Delta f}$ ($k_{\rm B}$ is the Boltzmann constant and $T_{\rm coil}$ the coil temperature). Under such conditions, the available SNR from the coil for a signal amplitude $e_{\rm coil}$ is:

$$\Psi_{\rm coil} = E_{\rm coil}/E^{\rm n}_{\rm coil} \ \propto \ N/R^{1/2}_{\rm coil}. \qquad (1)$$

The AC coil resistance $R_{\rm coil}$ depends on wire diameter, frequency, and winding details (e.g., wire separation) due to skin and proximity effects.[1] For a multi-turn, multi-layer coil of given shape and size, one can empirically find an optimum wire diameter and spacing for the available coil volume, and the corresponding number of turns, $N_{\rm opt}$, to maximize the coil SNR. This usually corresponds to a rather small fraction of the coil cross-section effectively carrying current. Up to about 1 MHz, the skin and proximity effects can be made negligible using a suitable litz wire, consisting of twisted strands of insulated wires [2, 23, 24, 25], which can occupy most of the available space in the coil volume. The AC resistance of the coil is therefore close to its DC value, $R_{\rm coil} = \rho l/\sigma \propto S_L/\sigma^2$ (S_L is the cross-section available for the winding; σ, ρ, and l are the cross-section, DC resistivity and total length of the wire, respectively). If the space available for the winding is fully occupied by current-carrying conductors, the maximum coil SNR is obtained and it does not depend on N since $E_{\rm coil} \propto N = S_L/\sigma$. In that case, the coil SNR only depends on S_L ($\Psi_{\rm coil} \propto \sqrt{S_L}$) and therefore is highest for a fully occupied winding volume. For a fixed value of S_L, hence of the SNR $\Psi_{\rm coil}$, the quality factor Q of the tuned coil is fixed and its (resistive) impedance at resonance, $R_{\rm res}$, scales with the number of turns (which in turn depends on σ) as:

$$R_{\rm res} = R_{\rm coil}Q^2 \propto N^2. \qquad (2)$$

For instance, at $f = 100$ kHz, $R_{\rm res}$ commonly lies in the range 1–500 kΩ, depending on coil shape and size. Equation 2 shows that the impedance of the tuned coil can be substantially varied without penalty for the coil SNR $\Psi_{\rm coil}$ by jointly changing the number of turns and the wire cross-section.

2.1.2 Preamplifiers and noise matching

We now consider the influence of the PA characteristics on the final SNR, after amplification. Any PA unavoidably adds noise to the detected signal. Its effect can be calculated using an electronic model of the PA (Fig. 2), comprising independent and uncorrelated input voltage and current noise sources, $e^{\rm n}_{\rm PA}$ and $i^{\rm n}_{\rm PA}$, characterized by the corresponding voltage and current rms noise densities, $E^{\rm n}_{\rm PA}/\sqrt{\Delta f}$ and $I^{\rm n}_{\rm PA}/\sqrt{\Delta f}$. The detection tank circuit consists of the coil (with inductance L and series resistance $R_{\rm coil}$) and the lossless tuning capacitor (its capacitance actually includes the input capacitance of the PA, see the caption of Fig. 2) .

The SNR reduction due to the PA is commonly quantified by the noise factor F, defined as the ratio of the noise *power* density at the output of the PA to that of an ideal noiseless PA (for which $E^{\rm n}_{\rm PA} = I^{\rm n}_{\rm PA} = 0$) with the

---

[1] The skin effect is the tendency for RF currents to flow on the surface of wires; the proximity effect is the tendency for currents to flow in other undesirable patterns due to the magnetic fields generated by currents in nearby wires.

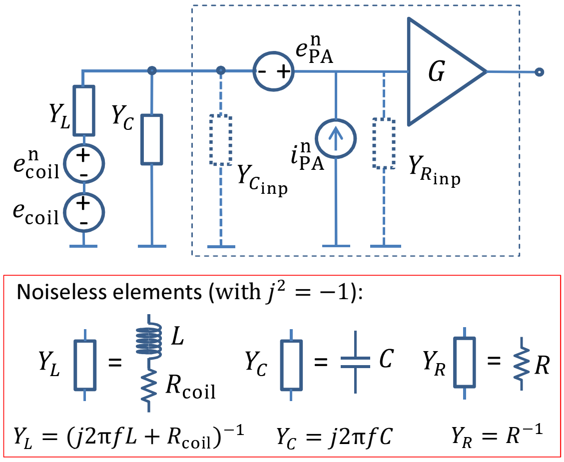

Figure 2: Electronic model of tank circuit and PA, represented as an ideal noiseless amplifier of gain G and infinite input impedance, together with a noiseless input resistance R_inp and capacitance C_inp. R_inp is usually so large that it is omitted. e^n_PA and i^n_PA are the PA voltage and current noise sources. For FET-based input stages, C_inp can be considered to lie on the left-hand side of the noise sources [26] and therefore simply modifies Y_C. These elements (the dotted R_inp and C_inp) will no longer be displayed in the following. e_coil and $e^\mathrm{n}_\mathrm{coil}$ are the signal emf and the Johnson noise in the PU coil. The correspondence between different lumped elements and admittance values is given below the model.

same gain. The reduced SNR at the output of PA is thus $\Psi = F^{-1/2}\Psi_\mathrm{coil}$.

It can be shown [27] that, in the absence of correlations between noise sources, the noise factor does not depend on R_inp and is given by:

$$F = 4k_\mathrm{B}T_\mathrm{coil}\Re(Z) + \frac{(I^\mathrm{n}_\mathrm{PA})^2|Z|^2 + (E^\mathrm{n}_\mathrm{PA})^2}{4k_BT_\mathrm{coil}\Re(Z)}, \tag{3}$$

where Z is the frequency-dependent impedance of the detection tank circuit, and therefore F is also frequency-dependent ($|Z|$ is maximum at resonance where $Z = R_\mathrm{res}$).

There is an optimal choice of signal source impedance for which the noise factor is minimized and Ψ is maximised. The so-called noise matching condition [27] is achieved for a purely resistive impedance, R_opt, such that:

$$R_\mathrm{opt} = E^\mathrm{n}_\mathrm{PA}/I^\mathrm{n}_\mathrm{PA}. \tag{4}$$

The corresponding optimal noise factor F_opt characterizes the noise performance of the PA. Amplifiers with front-end field effect transistors, rather than bipolar transistors with their flicker noise at low frequency [26, 28], are more suitable in terms of noise. They have values for R_opt in the range 10-800 kΩ, nominal input resistive impedances R_inp higher than 100 MΩ (large enough to be considered infinite here), and a small input capacitance which just slightly shifts the resonance of the tank circuit (see Fig. 2). Untuned PU coils have rather small impedances and they are reactive, therefore coil tuning is commonly used and allows for noiseless impedance transformation to approach the optimal condition $R_\mathrm{res} = R_\mathrm{opt}$ at which the best SNR performance would be achieved at the resonance frequency of the tuned PU coil.

As was shown in Sec. 2.1.1 (Eq. 2) one can vary the coil winding parameters (at fixed coil size) to adjust the tuned coil resonant impedance R_res to R_opt and thus meet the optimal SNR condition (noise matching) at the resonance frequency. One may alternatively increase R_res above R_opt in order to avoid a severe degradation of the out-of-resonance noise factor. This possibility is illustrated in Fig. 3, where F is plotted versus frequency for a set of values of $R_\mathrm{res}/R_\mathrm{opt}$ corresponding to different numbers of turns N in a coil having a fixed winding cross-section S_L and quality factor Q, and therefore a fixed coil SNR Ψ_coil.

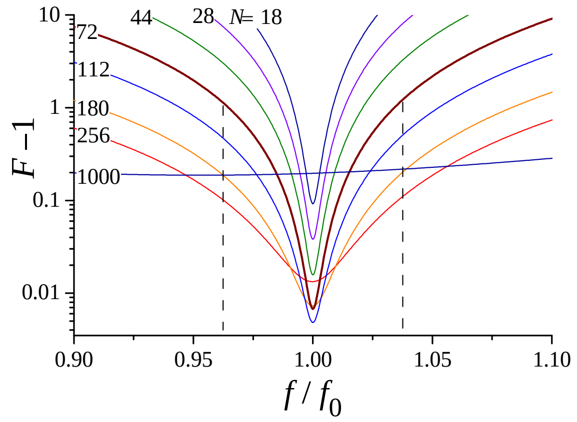

Figure 3: Computed noise factor F versus reduced frequency f/f_0 obtained at $T_\mathrm{coil} = 300$ K using Eq. 3, the noise parameters of the SR560 PA (App. A), and the impedance of tuned PU coils having different numbers of turns ($N = 18$–1000, $L = 0.255N^2$ μH), fixed $Q = 190$, $f_0 = 107$ kHz. $N = 72$ corresponds to the parameters of the 2×36-turns PU coil pair used for MRI in Sec. 3.4, with the vertical dotted lines marking the relevant frequency span. For this coil geometry, all N-values can be realised with commercially available litz wire, except $N = 1000$ for which the curve is shown for illustration only.

In principle, the lowest noise factor corresponds to a resistive signal source of optimal resistance (Eq. 4). For a tank circuit this can be satisfied only at resonance. However, Fig. 3 shows that a low value of the noise factor can be obtained over a broad frequency range, even when the impedance of the tuned coil is mostly reactive, without significant degradation of the SNR at the resonance frequency.

The idea of noise matching over some bandwidth by adjusting the coil impedance was already proposed by Hoult [17]. It can be used not only for convenience (there is no need to precisely tune the tank circuit to the operating frequency) but also for the detection of broadband signals for which broadband noise matching is needed to achieve a high SNR. This is the case in low frequency MRI for which the useful signal bandwidth (corresponding to the frequency span in the readout direction, see for instance Fig. 15 in Sec. 3) can be of the order of f_0/Q.

Other methods can be used to vary the impedance of the detection circuit seen by the PA. They imply noiseless impedance transformation schemes [29] which could also serve for noise matching. For instance, a simple and noiseless way to decrease the impedance seen by the PA consists in splitting the tuning capacitor (into two capacitors in series) and using the signal across one of them. Impedance transformation can also be applied even if an untuned PU coil with an almost fully reactive impedance is used for very broadband detection [30]. Of course, the general requirement for such broadband operation is to have a very low noise PA ($F_\mathrm{opt} - 1 \ll 1$). It can then operate in non-optimal conditions (being imperfectly noise matched with the detection tank circuit) without significant degradation of the SNR.

Once noise matching has been achieved, Eq. 3 shows that the PA input impedance R_inp does not influence the optimal noise factor and the final SNR (see also [31, 27] for details). This suggests a way to control the detection bandwidth and RD without noise penalty by manipulation of Z_inp with the use of FB schemes; this will be discussed in Sec. 2.2 and experimentally demonstrated in Sec. 3. We already draw attention on the fact that the actual detection bandwidth can be strongly modified by the direct connection to a PA even in the absence of deliberately implemented FB, due to undocumented internal FB loop(s) found in several PAs (see Sec. 3.1). This can be so pervasive that the implementation of an additional external FB may be required for an appropriate operation of the detection.

2.2 Feedback models

Two simple FB coupling schemes, easy to implement at low frequencies, are described here. The first scheme, described by Hoult [17], is frequently realised using a noiseless capacitor for the FB connection of Fig. 4a and will thus be referred to as FB with capacitive coupling. It will be used to model the internal FB in PAs evidenced in the results of Sec. 3.1. The second scheme, depicted in Fig. 4b and implemented in our experiments, will be called FB with inductive coupling because of the way the FB loop acts on the tank circuit. This scheme was shown to be efficient at high frequencies [9, 27, 32], although more delicate to implement than at low frequencies because of up- and down-frequency conversions.

Both coupling schemes belong to the first family of FB schemes in terms of the classification given in the introduction: they indirectly modify RD through changes in the response of the detection circuit. It will be shown that in a suitable high-gain limit both could be equivalently represented by adding an impedance in parallel to the tank circuit for any calculations of NMR signals. However, the impact of the two coupling schemes on RD is different. The well-known statement that FB does not affect the SNR follows from the above-mentioned fact that the SNR does not depend on the PA input impedance (Eq. 3 and Refs. [31, 27]); it only depends on the characteristics of the source and on the PA noise parameters.

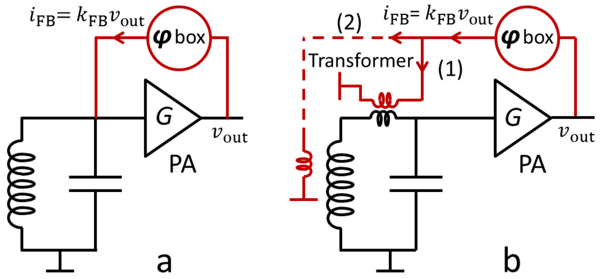

Figure 4: Capacitive (a) and inductive (b) FB schemes. The FB box φ_box is used to control the phase and amplitude of the current i_FB, proportional to the PA output voltage, which is fed back to the tank circuit. FB components are drawn in brown (color on line) in this and subsequent figures. Inductive coupling (b) is achieved through a transformer (path 1) or a coil coupled to the PU coil (path 2).

In the forthcoming derivations related to FB schemes the frequency dependence of the signal and noise components are evaluated within narrow enough frequency intervals ($f \pm \Delta f/2$, where $\Delta f \ll f_0/Q$), considering these components *as if* they were sinusoids [17, 27, 21, 33] of frequency f, with amplitudes such as e_coil and $e^\mathrm{n}_\mathrm{coil}$ (the emfs induced in the coil, proportional to the signal and noise spectral densities as well as to Δf and $\sqrt{\Delta f}$, respectively). This approach is required, for instance, in low-frequency MRI since signals with spectral widths broader than the bandwidths of high-Q detection circuits may be involved, contrary to the case of conventional MRI. With this approach, equations for voltages and currents are derived and solved conventionally, making use of complex impedances and complex time-dependent voltages and currents [17, 27, 21].

2.2.1 Capacitive coupling

In practice, this type of FB can be conveniently implemented using a "FB box" device to inject the FB current into the tank circuit (Fig. 4a). This box may be a transconductance amplifier, or voltage-controlled current source: $i_\mathrm{FB} = k_\mathrm{FB} v_\mathrm{out}$ with a complex transconductance coefficient k_FB (having adjustable phase and amplitude), as sketched in Fig. 12 of Sec. 3.

Alternatively, the FB box can be simply replaced with a suitable passive element of admittance Y^0_FB (usually a capacitor), as was done in the initial implementation [17]. In that case FB can also be schematically represented as in Fig. 4a with the parameter k_{FB} given by:

$$k_{\mathrm{FB}} = Y^0_{\mathrm{FB}}(G-1)/G. \tag{5}$$

An equivalent circuit corresponding to this FB scheme and including the relevant noise sources is shown in Fig. 5a. The input impedance of the PA is considered as infinite for simplicity, but its voltage and current noise sources, $e^{\mathrm{n}}_{\mathrm{PA}}$ and $i^{\mathrm{n}}_{\mathrm{PA}}$ are included. Y^0_{FB} is the (complex) admittance of the FB component. As mentioned in the introduction, using this type of FB is equivalent to modifying the input impedance of PA (R_{inp} in Fig. 2), as sketched in Fig. 5b in which the frequency dependent parameter α and admittance Y_{FB} are easily derived for full equivalence of circuits in terms of output voltage and current flowing in the tank circuit:

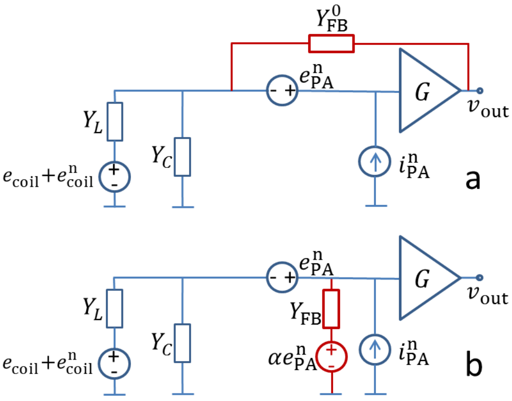

Figure 5: Simplified equivalent circuits modelling a PA with capacitive FB. a: directly equivalent circuit; b: equivalent circuit with a FB input admittance.

$$\alpha = 1/(1-G), \tag{6}$$
$$Y_{\mathrm{FB}} = Y^0_{\mathrm{FB}}\,(1-G)\,. \tag{7}$$

Note that the noise sources $e^{\mathrm{n}}_{\mathrm{PA}}$ and $\alpha e^{\mathrm{n}}_{\mathrm{PA}}$ are fully correlated since α is a constant, whereas other noise sources are uncorrelated. There is no degradation of the SNR if the FB element Y^0_{FB} is noiseless and reactive [17] and the effect of the source $\alpha e^{\mathrm{n}}_{\mathrm{PA}}$ is simply a small shift of the SNR optimum frequency compared to the open loop case of Fig. 3. Furthermore, it is shown in App. B.1 that $\alpha e^{\mathrm{n}}_{\mathrm{PA}}$ in Fig. 5b can be neglected for a well-designed system, for which at any frequency $\left|Y^0_{\mathrm{FB}}\right| \ll |Y_{\mathrm{L}} + Y_{\mathrm{C}}|$: FB acts in this case as a mere modification of the PA input impedance. Detailed considerations on the FB equivalent scheme of Fig. 5b and its additional noise sources are also given in App. B.1.

Equation 7 shows that if a capacitor is used as feedback element a gain with a phase shift close to $\pm\pi/2$ for $|G| \gg 1$ is needed to produce a frequency-shift-free change of the Q-factor with a resistive equivalent impedance at the input of the PA [17]. It also suggests that the effective FB input admittance is linear in G (the so-called Miller effect).

2.2.2 Inductive coupling

This type of FB loop is achieved when a FB emf is generated in the tank circuit either through a low-L inductive transformer connected in series with the PU coil [18] (path 1 in Fig. 4b) or directly in the PU coil from an additional weakly coupled loop [9, 32] (path 2 in Fig. 4b).

Although both coupling methods are electronically equivalent, their effects on the spin dynamics (the RD effects) could be different, because the loop used for path 2 produces an additional RF field in the sample which may be comparable or even stronger than that produced by the PU coil, depending on the geometry and orientation of this coupling loop. This can be used to actively increase the RD field without significantly affecting the effective Q-factor of the tuned PU coil when coil and loop are geometrically well decoupled. In that case the inductive coupling scheme can be included in the second family of FB schemes according to the classification given in the introduction. For simplicity, this direct action of current in the FB loop on the sample will not be considered in the remainder of this article.

A simplified equivalent circuit of Fig. 4b is displayed in Fig. 6a. It comprises a real PA with a possible internal FB represented by the admittance $Y^{\mathrm{int}}_{\mathrm{FB}}$, a tank circuit with coil and capacitor admittances Y_L and Y_C (Y_L has a real part due to losses in the coil), and an induced FB emf source proportional to the output voltage of the ideal PA, written as $e_{\mathrm{FB}} = kv_{\mathrm{out}}/G$. The coupling coefficient is $k = k_{\mathrm{FB}}MG$, where k_{FB} is the gain of FB transconductance amplifier and M is the mutual inductance of the inductive coupling in Fig. 4b. The more general case of inductive FB with a voltage amplifier and additional noise

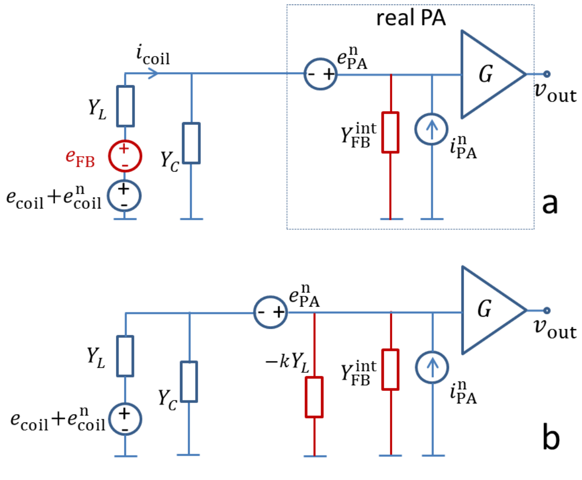

Figure 6: Simplified equivalent circuits modelling an inductive FB loop (Fig. 4b). a: Directly equivalent circuit for a real PA with some internal FB (Fig. 5b) at high gain ($\alpha \approx 0$). The inductive FB action is represented by the emf voltage e_{FB}. b: Equivalent circuit including the two FB loops (internal, capacitive and external, inductive) described in terms of PA input impedance.

sources in the FB loop is considered in App. B and it is shown that the simplified model of Fig. 6a is usually a good approximation to the real situation if the FB gain is large enough.

Considering Kirchhoff equations one can derive the voltage at the input of the ideal PA:

$$v_{\mathrm{out}}/G = \frac{(Y_L + Y_C)e^{\mathrm{n}}_{\mathrm{PA}} + Y_L\left(e_{\mathrm{coil}} + e^{\mathrm{n}}_{\mathrm{coil}}\right) + i^{\mathrm{n}}_{\mathrm{PA}}}{Y_L\left(1-k\right) + Y_C + Y^{\mathrm{int}}_{\mathrm{FB}}}. \qquad (8)$$

Equation 8 shows that the effect of an inductive coupling can be represented by the addition of the impedance $-(kY_L)^{-1}$ in parallel to $(Y^{\mathrm{int}}_{\mathrm{FB}})^{-1}$ (see Fig. 6b). The effect of the two FB loops is simply represented by the PA input noiseless admittance $Y_{\mathrm{inp}} = -kY_L + Y^{\mathrm{int}}_{\mathrm{FB}}$, therefore the added inductive FB does not affect SNR either. If no resonance shift occurs due to inductive FB (i.e., if kY_L is purely real), then one can define an effective Q-factor when the FB loop is closed, Q_{FB} as:

$$Q_{\mathrm{FB}} = Q_{\mathrm{OL}}\left[v^{\mathrm{FB}}_{\mathrm{out}}\left(f_0\right)/v^{\mathrm{OL}}_{\mathrm{out}}\left(f_0\right)\right], \qquad (9)$$

where Q_{OL} is the Q-factor with open inductive FB loop, $v^{\mathrm{FB}}_{\mathrm{out}}\left(f_0\right)$ and $v^{\mathrm{OL}}_{\mathrm{out}}\left(f_0\right)$ are the output voltages at resonance ($f = f_0$) for closed and open (k=0) inductive FB loop, defined from Eq. 8 with fixed e_{coil} and neglected noises.

Note that the model of Fig. 6b is correct in terms of output voltage, but, in contrast to capacitive FB, is incorrect for computing the current i_{coil} flowing through the coil and evaluating RD. Actually, this current is the sum of currents flowing in the coil branch and in the additional $-kY_L$ branch (this results from artificially splitting the coil admittance in two branches, see Eq. 45 in App. B.2). It can be found from Fig. 6a by applying Kirchhoff equation and using Eq. 8 with neglected noise:

$$i_{\mathrm{coil}} = \frac{Y_L(Y_C + Y^{\mathrm{int}}_{\mathrm{FB}})e_{\mathrm{coil}}}{Y_L\left(1-k\right) + Y_C + Y^{\mathrm{int}}_{\mathrm{FB}}}. \qquad (10)$$

Radiation damping rate and frequency pulling are proportional to the out-of-phase and in-phase parts of i_{coil} with respect to e_{coil}. If kY_L is purely real and negative, Q-damping occurs with no resonance frequency shift. At resonance, according to Eqs. 8 and 10, no frequency pulling occurs and only radiation damping exists with the rate:

$$\Gamma^{\mathrm{FB}}_{\mathrm{RD}} = \Gamma^{\mathrm{OL}}_{\mathrm{RD}}(Q_{\mathrm{FB}}/Q_{\mathrm{OL}}), \qquad (11)$$

where $\Gamma^{\mathrm{FB}}_{\mathrm{RD}}$ and $\Gamma^{\mathrm{OL}}_{\mathrm{RD}}$ are the radiation damping rates for closed and open loop operations, respectively. The RD rate for open loop operation can be computed as for a simple tank circuit (see for instance Ref. [34]).

Finally, note that it is possible to adjust the inductive FB so as to have:

$$-kY_L + Y^{\mathrm{int}}_{\mathrm{FB}} = 0, \qquad (12)$$

which allows for neutralisation preventing problems such as an onset of oscillations, resonance shape changes and frequency shifts otherwise resulting from internal capacitive FB. At the same time according to Eq. 10 neutralisation does not exactly recover the RD of the stand-alone tank circuit.

3 Experiments

3.1 Internal feedback of preamplifiers

When a high-impedance PA ($R_{\mathrm{inp}} \gg R_{\mathrm{res}}$) is used in low frequency NMR, it is expected to not affect the resonance characteristics of a tank circuit connected to its input port (see Fig. 1), apart from the trivial gain-independent frequency shift produced by the added input capacitance C_{inp}. Actually, this is not true and we found that for the very standard detection scheme represented in Fig. 7 with the direct connection scheme (a) to a single-ended input, all the commercial low-noise PAs that we have tested and that are commonly used for low-field NMR and MRI (listed in App. A) strongly affect (broaden, narrow and/or shift) the measured resonances, in a way that strongly depends on the gain of the PA. This is contrary to what one would expect since the input impedances of these PAs (up to 100 MΩ) are usually much higher than the impedance of the tuned PU coils (R_{res} ~100 kΩ for our room-temperature systems, see Sec. 3). More importantly, it is impossible to operate under certain conditions or with some devices because of the onset of electronic instabilities or oscillations. This was observed, for instance with the SR560 PA at non-inverting high gain ($G > 100$), and with the M5184 PA ($G = 1000$, non-inverting).

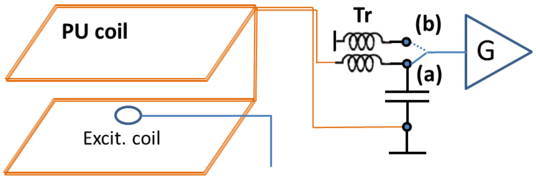

Figure 7: Two different connection schemes of the PA to the tank circuit were used. a: Direct coupling to the tank circuit; b: weak coupling through the low-inductance transformer Tr, shielded and not inductively coupled to the PU coil. The weakly-coupled excitation coil was driven by an RF current generator to induce an emf e_{coil} for measurements of response curves.

For a quantitative description of these unexpected observations, series of frequency-dependent signals were recorded for different PAs and gain values in a direct coupling configuration (Fig. 7, connection a). The Q-factor associated with the intrinsic losses in the tank circuit and the resonance frequency associated with its components ($f_0 = 1/2\pi\sqrt{LC}$) were reliably measured with the PA weakly coupled to the tank circuit (Fig. 7, connection b) as suggested in Refs. [2, 21].

Figure 8 displays typical response for a tuned PU coil directly connected to the SR560 PA for different gain values. Besides the broadening of resonances for increasing negative gains, significant shifts were observed.

A simple model of a tank circuit with a resistor R_{coil} in series with the coil was used to derive the expected amplitudes of signals for the direct coupling and weak

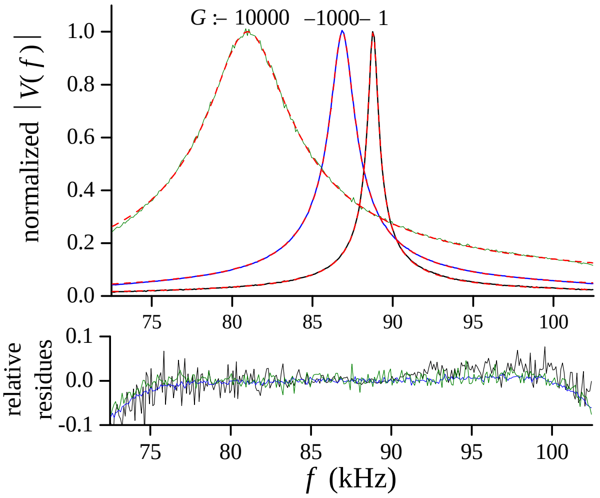

Figure 8: Examples of measured response signals with the direct coupling scheme (a) of Fig. 7 for G =-1, -1000, and -10000. The PU coil pair described in Sec. 3.5 was connected in series (L = 2.08 mH) and tuned close to 87.45 kHz. The fits by Eq. 13 (red dotted lines) yield Q' = 141.5, 60.3, and 16.6, respectively, instead of Q = 157 for a weak coupling measurement (not shown). Relative residues (lower plot) do not exceed 7% in the fitting frequency range.

coupling connections:

$$|V_{\mathrm{dir}}(f)| = A' \frac{f}{f_0'} \left\{ \left[1 - \frac{f^2}{f_0'^2} \right]^2 Q'^2 + \frac{f^2}{f_0'^2} \right\}^{-1/2} \quad (13)$$

$$|V_{\mathrm{weak}}(f)| = A \frac{f^3}{f_0^3} \left\{ \left[1 - \frac{f^2}{f_0^2} \right]^2 Q^2 + \frac{f^2}{f_0^2} \right\}^{-1/2}. \quad (14)$$

The quality factor of the tank circuit is defined as $Q = 2\pi f_0 L / R_{\mathrm{coil}}$; the RF generator is assumed to drive a frequency-independent current in the excitation coil, therefore a common f/f_0 factor appears in both measuring schemes due to the Faraday detection (with $e_{\mathrm{coil}} \propto f$). An additional $(f/f_0)^2$ factor is introduced for the weak coupling measurement scheme due to the use of a transformer (for an AC current i, $V_{\mathrm{dir}} \propto i/Cf$ and $V_{\mathrm{weak}} \propto if$).

Experimental resonance curves (such as in Fig. 8) were fit with the relevant function to extract modified resonance frequencies and quality factors. The notations Q' and f_0' were used for the fitted parameters of Eq. 13 on datasets from experiments performed in direct coupling, whereas Q, f_0, and Eq. 14 were used for the weak coupling scheme.

Although care must be taken when performing such measurements (e.g., by reducing inductive crosstalk between the excitation coil and the transformer and capacitive couplings between coils) in order to get good fits over a broad frequency range, the extracted fit parameters, Q' and f_0', were found to be quite robust against measurement imperfections as soon as $Q' \gg 1$ even if the experimental curves appeared unsatisfactorily fit. Excellent fits (by Eq. 13) were obtained for weak coupling measurements as well, with the same conclusions about the robustness of the measurement procedure.

Figure 9 shows results derived from measurements of Q' and f_0' as functions of gain G for the SR560 PA in the direct coupling scheme.

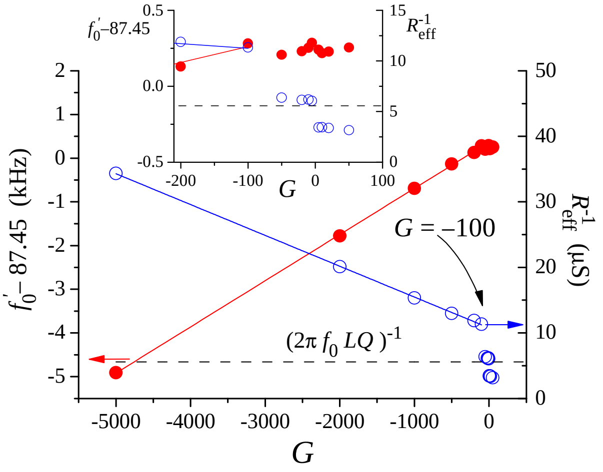

Figure 9: Measured resonance frequency f_0' (filled symbols) and effective admittance at resonance R_{eff}^{-1} (open symbols) of the directly coupled tank circuit as functions of the PA gain. The dashed horizontal line corresponds to the admittance at resonance of the weakly coupled tank circuit. The solid lines are linear variations consistent with a capacitive FB model (Eqs. 15 and 16). The inset displays the data obtained at moderate gain ($|G| \leq 200$) with expanded scales.

The parameters Q' and f_0' can be combined as the effective parallel resistance of a loaded tank circuit at resonance, $R_{\mathrm{eff}} = 2\pi f_0' L Q'$. The corresponding admittance R_{eff}^{-1} results from the addition of the admittances due to coil losses and to PA internal FB. With the latter given by Eq. 7 in a simple capacitive coupling model, the associated admittance would linearly depend on the gain as:

$$R_{\mathrm{eff}}^{-1} = (2\pi f_0 L Q)^{-1} + \Re\left[(1-G)\, Y_{\mathrm{FB}}^0\right]. \quad (15)$$

For most gain values R_{eff}^{-1} is much larger than measured for this tank circuit in the weak coupling mode of Fig. 7. The imaginary part of Y_{FB}^0 is expected to modify the resonance frequency as follows (in a first order approximation):

$$f_0' - f_0 = \pi f_o^2 L\, \Im\left[(1-G)\, Y_{\mathrm{FB}}^0\right]. \quad (16)$$

Linear variations of the measured resonance parameters are typical of the presence of capacitive FB and could be described by the Miller effect (see Ref. [17] and Sec. 2.2.1). However, the gain dependence of R_{eff} in Fig. 9 has strikingly different variations at high and low negative gains, below and above a border gain $G = -100$. At moderate gain values ($|G| < 100$, inset in Fig. 9), R_{eff}^{-1} is observed to have a step-like variation with gain which cannot be described by Eq. 15, with negligible broadening for all negative gains and constant significant narrowing for positive gains, while f_0' displays no clear variation. On the contrary, both f_0' and R_{eff}^{-1} linearly vary with G for large negative gains ($G < -100$). We believe that this may be explained by a modification in the FB loop or the addition of a second loop coupling different stages of the PA to its input. This possibility is considered in App. B.3, where equations analogous to Eqs. 6 and 7 are derived and it is shown that several FB loops can be still represented by an input FB impedance as in Fig. 5b. In that frame, Eq. 15 could be replaced with a more complex variation involving two FB admittance parameters:

$$R_{\text{eff}}^{-1} = (2\pi f_0 L Q)^{-1} + \Re\left[(1 - G_1)\, Y_1 + (1 - G)\, Y_2\right]. \quad (17)$$

Assuming that the PA comprises a first stage with fixed gain $G_1 = -100$, Eq. 17 can indeed be used to describe the high-gain regime in Fig. 9 with fixed parameters Y_1 and Y_2 (for simplicity, we assume G to be real and include the phase shift of the PA in Y_2). Similarly, Eq. 16 could be replaced with the equation involving the same two-parameter effective admittance as Eq. 17. The slopes observed in Fig. 9 for the shift and the effective admittance yield $\pi f_o^2 L \Im\left[Y_2\right] = 1.06$ Hz, therefore $\Im\left[Y_2\right] = 21$ nS, and $\Re\left[Y_2\right] = 4.7$ nS, respectively. Finally, $\Re\left[Y_1\right] = 51$ nS is evaluated from the data using Eq. 17 for $G = G_1 = -100$, but the reactive part of Y_1 cannot be reliably inferred from the data due to the frequency shift resulting from the PA static input capacitance (f_0 differs from the value of f_0' obtained for $G = 1$, contrary to Eq. 16).

In the weak coupling scheme, Q and f_0 (not displayed in Fig. 9) are found to be independent of G, as expected, and therefore reflect intrinsic characteristics of the tank circuit. In direct coupling tests with minimal gain $G = \pm 1$ modified quality factors bracketing the Q-factor of weak coupling measurements were found, with a moderate relative difference. This indicates that weak internal FB occurred in that case and provides an approximate method for evaluating intrinsic quality factors of resonant tank circuits in direct coupling connection, but the accuracy of the method is limited (see the inset in Fig. 9). The resonance frequency in that case was indeed slightly lowered compared to weak coupling measurements due to the static input capacitance of the PA (25 pF).

An external FB loop, described in the next section, could be used to compensate for the ill-controlled effect of the observed internal FB. This technique is known in electronics as neutralization [27].

Interestingly, internal FB was found to be strongly reduced when the SR560 PA was operated in differential mode (the other tested PAs only have single-ended inputs). Figure 10 shows that for a symmetric detection system (square symbols) OL operation was stable for all gain values and changes in Q', R_{eff}, and f_0' were reduced more than ten-fold with respect to single-ended operation (Fig 9). A possible compensation mechanism of internal FB in differential mode is proposed in App. B.4. It predicts that imbalance in the lengths (i.e. capacitances and associated admittances Y_{A} and Y_{B}) of the connecting cables introduces internal FB with a linear term in G and $Y_{\text{A}} - Y_{\text{B}}$ (Eqs. 91 and 100 in App. B.4). This is indeed observed at large gain ($G > 100$) for a set of cable lengths (e.g., 1 m vs. 1.5 m for the triangles in Fig. 10). Such data yield values for the internal FB admittances Y_0 for the model of App. B.4 and provide a scale for the required symmetry of the detection system: a few cm, or a few pF imbalance can be tolerated.

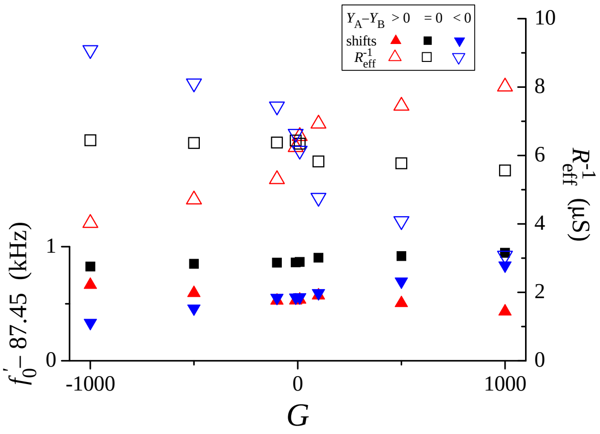

Figure 10: Measured resonance frequency f_0' (filled symbols) and effective admittance at resonance R_{eff}^{-1} (open symbols) of the directly coupled tank circuit as functions of the gain of a SR560 PA used in differential mode.

3.2 Implementation of inductive FB

A minimal system designed to achieve a flexible control of FB strength should comprise a phase rotator and a FB element. Capacitive and inductive FB schemes could in principle both be implemented at low frequencies but there are practical difficulties with capacitive FB. Typical cm- to dm-size tank circuits for MRI and NMR around 100 kHz have impedances at resonance $R_{\text{res}} \approx 100$ kΩ. To reduce their Q-factors ten-fold or more, the effective FB impedance must be resistive with $(Y_{\text{FB}})^{-1} \lesssim 10$ kΩ (the notations are those of Fig. 5). To avoid significant additional noise arising from the FB loop the gain of the PA must be high enough, e.g. $|G| \gg 10$, which leads to $\left|(Y_{\text{FB}}^0)^{-1}\right| \gg 100$ kΩ, corresponding to a FB capacitor with $C_{\text{FB}} \ll 16$ pF. This capacitance is quite small and when commercial PAs are used the FB elements and connecting cables must lie outside the PA: significant stray capacitance of cables and connectors unavoidably induce stability and reproducibility issues. This is especially critical when positive FB is used to increase Q-factors for enhanced RD because very small changes in Y_{FB}^0 significantly modify resonance shapes near oscillation thresholds.

Technically, inductive FB schemes are intrinsically more stable because the FB current flows in a low impedance transformer. Moreover, inductive FB can easily be used in combination with an impedance transformation network in the input of the PA since the FB signal is directly induced in the tank circuit and is not affected by the way PU coils are connected to the PA. For these reasons, we chose to use an inductive coupling scheme to feed a suitably amplified phase-adjusted signal back into the tuned PU coils of our low-field NMR systems. In our implementation (Fig. 11) differential operation and symmetry with respect to the ground of the coupling transformer and PU coils allowed for stable FB operation with strongly reduced internal FB and negligible added interference noise.

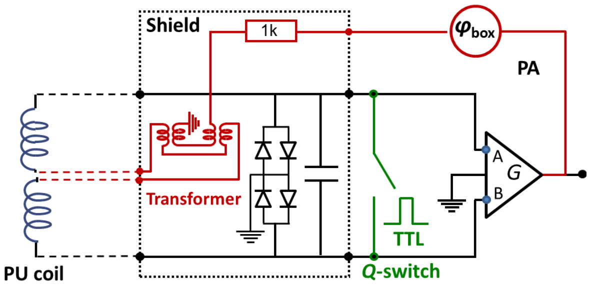

Figure 11: Elements of the NMR detection system with external inductive FB. The coupling transformer had a small self-inductance compared to that of the detection coil (1/100th). An additional Q-switch based on an ultra-low charge injection ADG636 CMOS switch was connected in parallel with the tank circuit to shorten ring-down just after RF pulses (FB does not operate when the PA saturates, [18]). Clamping diodes provide protection for the PA inputs and contribute to symmetry with respect to the ground, also enforced by balanced coaxial cables lengths to the inputs.

The FB control box was built using standard low frequency electronic circuitry (Fig. 12) and comprised a phase rotator to change the phase of the FB current in the loop quite independently of its amplitude. It allowed for the fine phase tuning needed for instance to meet the Nyquist stability criterion at high positive FB gain. The series resistor used to transform the output amplifier in Fig. 12 in a current generator was mostly located close to the transformer (see Fig. 11) to reduce the effect of the capacitance of connecting cables on FB phase stability.

The additional noise contribution from the elements in this FB loop (the noise from the amplifiers and the Johnson noise of the resistors) are evaluated in App. B.2. They are negligible compared to the coil and PA noise, which makes this system suitable for use without degradation of the PA noise factor.

The practical method used to modify effective Q-factors while keeping resonance frequencies unchanged consisted in finding the suitable phase at low gain for which gain changes induced negligible shifts of the resonance. This phase setting was usually accurate enough for operation over a broad range of gain values. Since the dynamic range of the FB loop was only limited by the non-linearity and saturation of the PA its output was monitored over a broad frequency range.

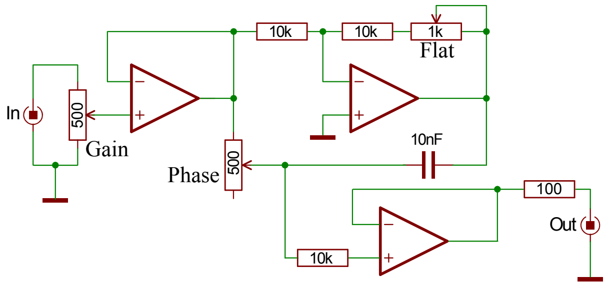

Figure 12: Electronic circuit of the φ_{box} used in the experiments. The “Flat” adjustment allows for independent control of “Gain” and “Phase” $(0-\pi)$ via 10-turns potentiometers of low enough resistance to induce negligible phase shifts below 200 kHz. Standard operational amplifiers (TL081) were used. Two identical circuits were implemented on the same printed circuit board. They could be chained for a wider phase shift range or independently used for active coil decoupling (Sec. 3.5).

3.3 Control of radiation damping

We use inductive FB to study the influence of distant dipolar fields (DDF) on NMR dynamics in highly polarised liquids [35, 36, 37] and in particular the complex interplay between RD and DDF which results for instance in multiple maser emissions [38]. In our low temperature experiments, the PU coil was a pair of saddle shaped windings connected in series, 3.4 cm long and 1.7 cm in diameter, with 30 turns each of 60-μm-diameter enamelled copper wire ($L = 0.14$ mH). With the tuning capacitor and coupling transformer sufficiently distant from the sample, a Q-factors of 7 only was achieved at 74 kHz due to resistive losses in connecting cryogenic coaxial cables, therefore the effects of the internal FB of the SR560 PA were negligible. Inductive FB was used to obtain a broad range of effective Q-factors ($1 < Q_{\text{FB}} < 100$), and therefore an easy adjustment of RD strength, which was convenient both for studies of NMR dynamics and maser emissions at high Q_{FB} and for studies of RD-free DDF-controlled dynamics at very low Q_{FB}. This is illustrated in Fig. 13 which displays typical free induction decay (FID) signal amplitudes from hyperpolarised ^{3}He in a liquid ^{3}He-^{4}He solution at 1.3 K for small flip angle RF pulses. In the main plot, the growing (decaying) signal recorded with positive FB (Q_{FB} =53) corresponds to a spin system in an unstable (stable) state. With moderate negative FB (Q_{FB} =4.2) signal decay was less strongly affected by RD.

The growth or decay of FID signal amplitudes at early times was clearly exponential (lower inset in Fig. 13), and exponential fits to the data yield signal decay rates for

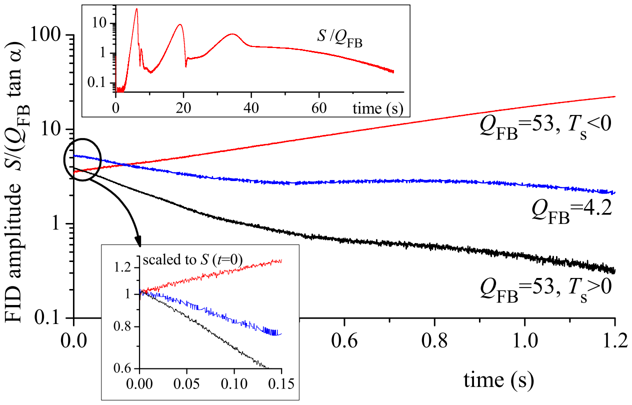

Figure 13: Time evolutions of FID signal amplitudes successively recorded from a highly polarised liquid ^{3}He-^{4}He sample (prepared from optically polarised ^{3}He gas, see [35]). Main plot: scaled signals for small flip angle pulses ($\alpha = 9°$ for positive spin temperature T_s, $\alpha = 4.8°$ for $T_s < 0$) and two Q_{FB} values corresponding to two FB adjustments. $T_s < 0$ was obtained using an inverting π pulse. The recorded signal amplitudes S (in units of the NMR console) are scaled for comparison of initial magnetisations (decreasing due to T_1 decay between pulses). Lower inset: zoom on the rescaled initial time evolutions. Upper inset: long-term signal evolution from another liquid sample with $T_s < 0$ and high Q_{FB}; irregular maser operation was observed.

a near-longitudinal magnetisation. In usual RD-driven conditions (for negligible DDF), these rates can be written

$$\Gamma = R_2 \pm \Gamma_{RD}^{FB} \tag{18}$$

where R_2 is the RD-free decay rate of FID signals and Γ_{RD}^{FB} is the RD rate, which is proportional to the coil filling factor, to Q_{FB}, and to the magnitude M_0 of the magnetisation [34]. M_0 is proportional to $S_0/\left(Q_{FB} \tan\alpha\right)$, where S_0 is the initial FID signal amplitude following a flip angle α, and the sign in Eq. 18 is that of the spin temperature. The rates inferred in the examples displayed in Fig. 13 are found to significantly deviate from Eq. 18, contrary to rates measured in similar experiments performed in low-density or weakly-polarised samples for which DDF are very weak.

In addition, an example of long recording of the signal amplitude evolution at high Q_{FB} with unstable magnetisation is displayed in the upper inset in Fig. 13. In the absence of initial RF flipping pulse, noise-triggered maser onset occured after a few seconds and was followed by a series of signal bursts instead of the expected single maser emission which usually reveals magnetisation reversal. This non-standard behaviour further reveals the strong effect of DDF on NMR dynamics.

Discussing the effects of DDF on initial signal growth or decay rates and of complex maser dynamics lies beyond the scope of this article and a comprehensive study will be reported elsewhere. This study was enabled by the systematic use of inductive FB for convenient control of variable RD rates.

In spite of the fact that the SNR in a carefully designed detection system is independent of the presence of FB, the actual SNR for the signals in Fig. 13 acquired with two different Q-factors were different because (i) the signals corresponding to Q_{FB}=53 were filtered by the narrow bandwidth of the detection, and (ii) the signal corresponding to Q_{FB}=4.2 was affected by digitization (the rms of the noise was lower than one bit of digitizer). This difference was not due to the use of FB and the low-Q_{FB} SNR would be improved by signal amplification outside the FB loop and by appropriate data filtering.

3.4 Increased bandwidth, faster recovery

We also systematically use inductive FB in low-field MRI research [39, 40] performed at room temperature with a compact home-built MRI setup. It is typically operated up to 3 mT, which corresponds to Larmor frequencies f≈97 kHz for ^{3}He NMR and f≈128 kHz for proton NMR, the two nuclei used in the experiments. Combining litz wire in detection coils with low-loss capacitors, Q-factors typically range from 100 to 200 depending on coil details. The PU coil used for the MRI experiments reported in this section comprised two 6×15 cm^2 rectangular windings, separated by a 4.2-cm gap, with 36 turns each of 25×0.1-mm litz wire. They were connected in series ($L = 1.32$ mH) and tuned for operation at 107 kHz.

The Larmor frequency span caused by imaging gradients over the field of view commonly reaches 10 kHz. This is not an issue in high-field, high-frequency MRI, even with high Q-factors, but in low field MRI this bandwidth can be a significant fraction of the Larmor frequency and very low Q-factors are therefore needed to avoid signal filtering by the detection coil. Strong negative FB was therefore used to achieve broadband detection.

Another important advantage of using inductive FB was the fast recovery of the detection circuit. Inductive FB used jointly with an electronic Q-switch significantly reduced dead-time after RF pulse excitations [18]. Following the fast initial ring-down induced by the closed switch ($R_{ON} \approx 40\ \Omega$), rapid damping of the emf caused by the 1–2 pC charge injection of the opening switch was enforced at low Q_{FB}. This allowed using MRI fast pulse sequences, with acquisition periods as short as 2 ms [39].

Examples of 2D projection MR images of a water sample obtained with and without strong external negative FB are shown in Fig. 14. The field-of-view for these images in the z-axis direction of the applied readout gradient corresponds to a 8.3-kHz frequency span, much broader than the bandwidth of the detection coils. With a FB-free $Q = 190$, measured in weak coupling mode (see Fig. 7), their filtering profile (the blue dotted line in Fig. 14a) would significantly attenuate image intensity of most parts of the sample. With the efficient damping of the strong FB used in this MRI demonstration (Fig. 14a,

$Q_{\mathrm{FB}} = 3.7$), the filtering profile was quite flat (the red dashed line) and therefore the image intensity was uniform over the sample.

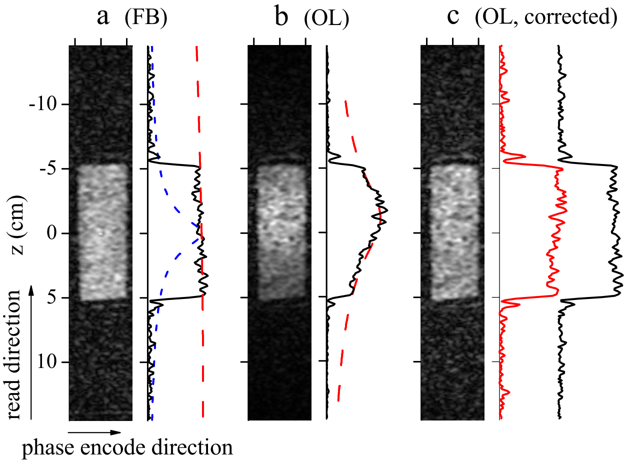

Figure 14: 2D images of a $10 \times 4 \times 4$ cm^3 CuSO$_4$-doped water sample obtained using a spin-echo MRI sequence with (a) and without (b) negative FB (spin-echo sequence managed using a Tecmag Apollo LF console: 90° flip angles, T_{obs}=30 ms, G_{read}=0.675 mT/m, i.e. 287 Hz/cm; NE=24, NR=500, TR=150 ms$\approx T_1$). 1D projections of the images onto the z-axis (black curves on the r.h.s. of the images) were obtained by suitable averaging in the phase encode direction. The dashed and dotted lines are measured electronic frequency responses of the detection. a: blue dotted line for weak coupling ($Q = 190$), red dashed line with FB ($Q_{\mathrm{FB}} = 3.7$). b: red dashed line for OL, with internal FB of the PA ($Q' = 133$). c: intensity-corrected image b (see text), with its 1D projection (red curve); that of image a (black) is displayed for comparison.

Figure 14b displays the image obtained without external FB. Despite the damping effect of the internal FB of the PA (the sign of G was chosen to decrease the Q-factor to 133, not to increase it), the image intensity was severely attenuated near its edges along the z-direction of the readout gradient. The black solid curves on the right of the images are the scaled 1D projections along the x-direction of the image intensities; they are consistent with the corresponding filtering curves (red dashed lines) of the detection circuits.

The image distortion in Fig. 14b can indeed be corrected while processing MRI data [41, 42]: this yields the image and 1D projection of Fig. 14c. They display a fairly z-independent noise level consistent with the noise factor for this coil: $F < 2.2$ over the field of view, $F < 1.15$ over the sample (see Fig. 3). This noise level is very close to that obtained with negative FB, as expected. However, the rather large applied correction leads to artifacts in the image (a distorted amplitude and enhanced edge artifacts are visible on the side-by-side profiles in Fig. 14c).

3.5 Coil decoupling for parallel imaging

Strong negative FB has been shown in the previous examples of applications to (i) strongly reduce currents wich result from the sample-induced emfs in PU coils (and therefore RD, see Sec. 3.3) and to (ii) increase detection bandwidth and therefore facilitate low-field MRI (Sec. 3.4). Both effects can in fact be beneficial for parallel imaging using separate coils having different sensitivities to different parts of the sample: negative FB automatically provides an active decoupling of the coils by blocking currents and the associated crosstalk [12].

This was demonstrated using an MRI setup similar to that of Sec. 3.4. Two rectangular PU coils (7.5×10.5 cm^2 windings separated by a 4-cm gap, 72 turns each of 25×0.1-mm litz wire, $L = 0.95$ mH) were *separately* tuned close to $f_0 = 87$ kHz with individual Q-factors $\approx$130 instead of being connected in series (with a total $L = 2.08$ mH) as in Sec. 3.1.

Figure 15 displays resonance curves for one of the coils while the other coil is not tuned. They were recorded for a series of negative FB strengths with the phase adjusted for shift-free operation of FB, therefore the resonance frequency f_0' did not depend on the gain. For moderate broadening the resonance curves were fit as described in Sec. 3.1 and the damped Q-factor Q_{FB} was the value of the fit parameter Q' in Eq. 13. For broad resonances Q_{FB} was inferred from signal amplitudes at resonance with and without the inductive FB loop using Eq. 9. A wide range of Q-factors was obtained and a flat response was achieved over the bandwidth needed for MRI at high gain. The inset in Fig. 15 shows that Q_{FB}^{-1} scales as the FB loop gain, as expected.

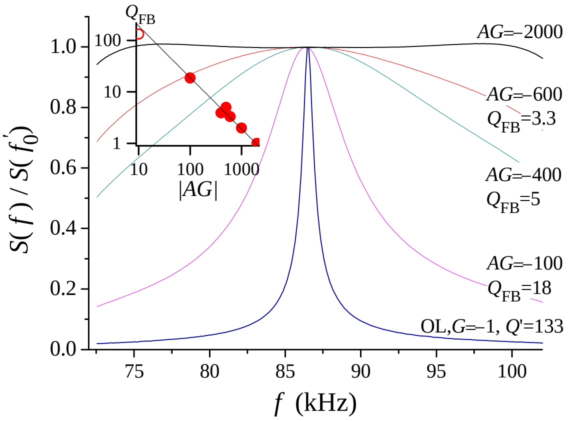

Figure 15: Main plot: selected resonance curves of *one* tuned coil with applied negative FB for a set of gains $|AG| = 1$–2000, combining the PA gain G and the φ_{box} input attenuation A (see Fig. 12). The curve with $Q' = 133$ corresponds to OL operation with $G = -1$ for which the internal FB of the PA was moderate. Inset: plot of Q_{FB} vs. gain (solid symbols). The line is a guide for the eye of slope -1 in log. scales. The OL value Q' is displayed as an open symbol for $G = -10$ (internal FB is the same as for $G = -1$).

To enforce active decoupling of the two tuned coils for MRI operation, a FB system was used for each coil. Figures 16a and b display the frequency variations around the common tuning frequency of signals from the two PU coils when an emf was induced in one of them. The coil signals were acquired using the two channels of a Tecmag Apollo console. Without FB (a) the strong coupling split the resonance in two modes of similar amplitudes with strongly correlated currents in the coils. With strong negative FB (b) a flat frequency response was obtained and signal from the driven coil (solid line) was much larger than from the passive coil (dashed line).

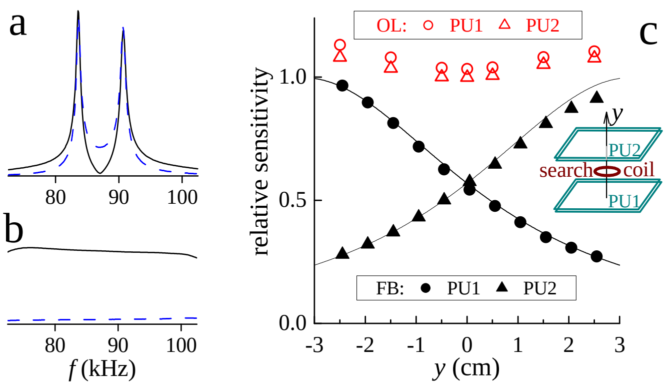

Figure 16: Signal amplitudes from PU coils *separately* tuned to the same frequency f_0. Frequency response measured in open loop (a) and with strong negative FB (b); an emf was electrically driven in the PU1 circuit using an additional transformer winding, without direct influence on the PU2 circuit. c: signals obtained when emfs are induced by a small search coil as functions of its position (symbols, see text) and computed on-axis sensitivities of individual coils (solid lines).

Figure 16c displays the measured axial sensitivity maps of the coils, i.e., the signal amplitudes recorded when a transmitting search coil was displaced along the y-axis of the coils. For open-loop operation (open symbols) excitation was performed at the low-frequency resonance in the doublets of Fig. 16a which corresponds to in-phase coupled currents in the PU coils. Both coils provided similar position-insensitive signals. This near-uniform sensitivity, similar to that of the series tank circuit, resulted from the very strong inductive coupling. When negative FB was used, the coils provided position-dependent signals (filled symbols) corresponding to their computed on-axis geometric sensitivities (solid lines): efficient decoupling was achieved.

This elementary coil-array allowed for parallel data acquisition with a field of view (FoV) smaller than the object for accelerated imaging. Fig. 17 displays an example of 2D projection MR imaging of a water sample with a 1.5-mm in-plane resolution and a 3-cm FoV in the vertical direction, smaller than the sample, obtained using 20 phase-encoding steps. The sensitivity encoded (SENSE) information obtained from the independent coils was used for image reconstruction with the computed (complex) 3D sensitivity maps of the coils [43]. The artifact-free final (unfolded) image in Fig. 17c demonstrates the efficiency of the decoupling scheme.

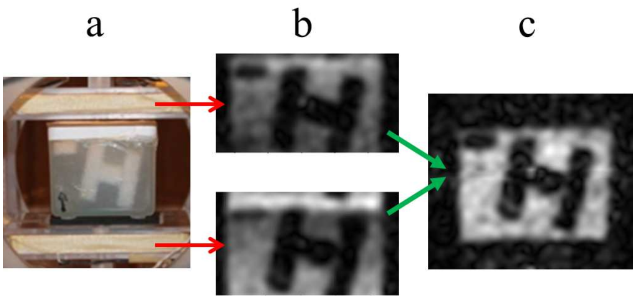

Figure 17: a: photograph of a 4.5×4.5×3.5 cm^3 doped water sample with Styrofoam shapes between horizontal PU coils. b: folded images from the FB-decoupled PU coils (imaging parameters as in Fig. 14 except T_{obs}=25 ms, NE=20, and NR=2250). Right: image reconstructed using the computed sensitivity maps of the coils.

Since the FB settings are independently adjusted for each coil, this efficient coil-decoupling scheme is conveniently scalable for arrays with a larger numbers of coils, and the settings would be immune to coil loading.

4 Discussion and conclusion

Noise matching a high-Q tuned detection coil and a front-end signal PA is an important issue to achieve high SNR in low-frequency NMR and MRI. This can often be achieved without matching networks through careful design, by varying the number of turns of the coil in the available winding volume to tailor the impedance of the tank circuit. This approach can be used either for noise matching at resonance only or over any desired bandwidth for broadband detection (for instance in MRI applications).

The bandwidth of the detection system is an independent but not less important issue, more critical than at high frequencies. Following the pioneering work performed by Hoult [17] and Brokaert [9], we have systematically evaluated the potential of electronic FB to actively tailor the detection bandwidth of tuned coils without noise penalty. This was done for two kinds of FB coupling between the PA output and the coil, with direct current injection (the so-called capacitive coupling), or via a transformer. The second configuration, or inductive coupling, is more easily implemented and offers a higher degree of control of the bandwidth as well as of the RD effects resulting from currents in the detection coil.

A key experimental finding reported in this work is the systematic observation of strong changes in the resonance characteristics of tuned coils when they are connected to different types of low-noise PAs. The usual configuration for low frequency Faraday detection: a tuned PU coil directly connected to a high impedance PA can lead to gain-dependent effects on signal response (broadening or narrowing and shift of electronic resonance) or even to an unstable situation (oscillations) which we associate with internal FB. One would for instance be trapped having lower SNR than expected when naively operating at a shifted resonance frequency measured in that configuration. One must also pay attention to uncontrolled internal FB whenever signal calibration or RD should be under control; for instance one must never measure NMR signals and electronic response at different PA gain. The intrinsic parameters of a tank circuit must be always measured in a weak coupling regime in which the PA is used to detect signals across a small coil weakly coupled to the PU coil, or one should at least reduce the gain of the PA to unity and check the effect of a change of gain polarity (if possible) to perform characterisations in an NMR detection configuration. Only such measurements can provide reliable estimations of parameters of the free probe. Splitting the total gain factor between two PAs in series and using well-balanced differential amplification were both shown to usually reduce internal FB, but never to a negligible level.

A carefully designed external FB loop can be used to remove the unwanted effects of PA internal FB (and even oscillation problems), as well as to flatten the signal response over large bandwidths and reduce ring-down times in the coil after RF pulses for MRI applications. This was evidenced by comparing images of a water phantom acquired with and without inductive FB. The additional benefit resulting from the suppression (or enhancement) of currents in the detection coil was demonstrated in an experiment performed on hyperpolarised liquid helium: RD was easily controlled by modifying the effective Q-factor of the probe for applications requiring maser conditions or, on the contrary, when RD or cavity pulling must be strongly reduced, for instance for very precise NMR frequency measurements. Finally, suppression of currents in coils via strong negative FB was also shown to allow performing active coil decoupling for parallel acquisition in MRI. A detailed description and discussion of the results of these various experiments falls beyond the scope of this article. They are reported to demonstrate that active FB using an inductive coupling scheme is a flexible tool to optimise NMR acquisition and control radiation damping in a wide range of situations in low-frequency NMR or MRI.

Acknowledgements

This work was supported in part by the FPGG (P.-G. de Gennes) foundation and the IMAGINE project of the French National Research Agency (ANR-12-IS04-0006).

A List of tested preamplifiers

In this work we have compared the NMR operation and performance of four low-noise commercial PAs and of one in-house instrumentation PA based on a front-end AD745 operational amplifier.

- The SRS560 PA (Stanford Research Systems, Inc. Sunnyvale, CA, USA) has a differential input and a wide choice of gain values. Its front-end stages are based on the LSK389 dual JFET component.
- The Model 5184 PA (Signal Recovery, Oak Ridge, TN, USA) is a single-ended input, fixed gain PA. Due to its large positive gain, it is difficult to achieve stable operation in NMR without neutralization by external negative FB.
- The SA220-F5 PA (NF Corporation, Yokohama, Japan) is a single-ended input, fixed gain PA. It appears to be less prone to oscillations with a high- Z tank circuit than the 5184 PA but still normally requires external negative FB for safe operation.
- The HMS-566 PA (formerly produced by DL Instruments, LLC, Brooktondale, NY, USA) is a typical low-noise PA suitable for a medium source impedance (also with a single-ended input).
- The AD743 and AD745 operational amplifiers combine a very low noise and a high noise-matching resistance (Analog Devices, Inc, AN-940 Application Note: *Low Noise Amplifier Selection Guide for Optimal Noise Performance*). They are used, for instance, in the input stages of several types of DSP lock-in amplifiers manufactured by Signal Recovery.

	R_{inp}	C_{inp}	G	R_{opt}	V_{n}
Model	MΩ	pF		kΩ	nV/$\sqrt{\text{Hz}}$
SR560	100	25	± 1–$5\,10^4$	30	4 max
M5184	5	50	1000	10	0.8 typ
SA-220F5	1	57	400	2.5	0.5 typ
HMS-566	0.1	n.a.	100-1000	0.4	1.2 typ
AD745	>100	20		200	2.5 typ

Table 1: List of the tested PAs and of their most relevant characteristics at 100 kHz.

B Full circuit equivalences

In this Appendix the electrical equivalences of circuits with capacitive and inductive FB coupling are derived, including all relevant noise terms. The high-FB-gain limits are discussed, which yield the simplified models used in Sec. 2.2.

B.1 Capacitive coupling

The FB scheme with generalized capacitive coupling of Fig. 4a is modelled by the directly equivalent circuit sketched in Fig. 18a. We have chosen to retain the separate elements of the tank circuit in the model instead of replacing them with their total admittance and the suitably transformed source term. This replacement is often done for simplicity, but we prefer keeping track of the current in the coil to facilitate the evaluation of RD effects (not detailed here).

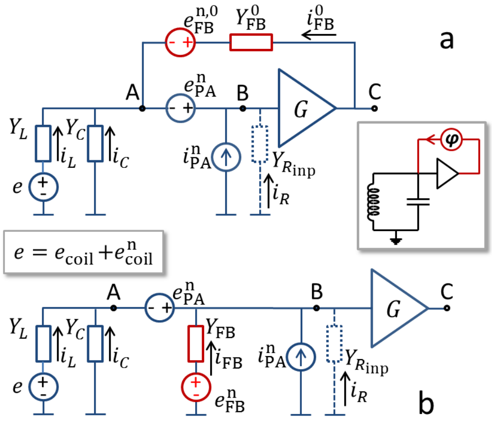

Figure 18: Two equivalent model circuits of the generalised capacitive FB scheme (see the inset) introduced in Sec. 2.2.1. The total source $e = e_{\mathrm{coil}} + e^{\mathrm{n}}_{\mathrm{coil}}$ in the PU coil branch consists of the signal emf and the coil Johnson noise. In these models, a finite input resistance R_{inp} of the PA is included for completeness (for one of the tested PAs, $R_{\mathrm{inp}} = 100\ \mathrm{k}\Omega$). The noise and admittance in the FB loop are $e^{\mathrm{n},0}_{\mathrm{FB}}$ and Y^0_{FB} (circuit a); their equivalent parameters in the PA input are $e^{\mathrm{n}}_{\mathrm{FB}}$ and Y_{FB} (circuit b).

The four currents considered in the model can be expressed as functions of voltage values at points A, B, and C in Fig. 18a:

$$i_L = -Y_L\left(v_{\mathrm{A}} - e\right) \tag{19}$$

$$i_C = -Y_C v_{\mathrm{A}} \tag{20}$$

$$i_R = -Y_{R_{\mathrm{inp}}} v_{\mathrm{B}} \tag{21}$$

$$i^0_{\mathrm{FB}} = Y^0_{\mathrm{FB}}\left(v_{\mathrm{C}} - v_{\mathrm{A}} - e^{\mathrm{n},0}_{\mathrm{FB}}\right)\ . \tag{22}$$

Using the constraints on current and voltage values:

$$-i_{\mathrm{FB}} = i_L + i_C + i_R + i^{\mathrm{n}}_{\mathrm{PA}} \tag{23}$$

$$v_{\mathrm{B}} = v_{\mathrm{A}} + e^{\mathrm{n}}_{\mathrm{PA}} \tag{24}$$

$$v_{\mathrm{C}} = G v_{\mathrm{B}}, \tag{25}$$

the output voltage is expressed as a function of the total emf e in the PU coil and of the PA and FB loop noise sources:

$$v_{\mathrm{C}} = G\frac{Y_L e + \left(Y_L + Y_C + Y^0_{\mathrm{FB}}\right) e^{\mathrm{n}}_{\mathrm{PA}} + i^{\mathrm{n}}_{\mathrm{PA}} - Y^0_{\mathrm{FB}} e^{\mathrm{n},0}_{\mathrm{FB}}}{Y_L + Y_C + Y_{R\mathrm{inp}} + Y^0_{\mathrm{FB}}\left(1 - G\right)}. \tag{26}$$

The circuit sketched in Fig. 18b is characterised by similar equations, with Eq. 22 replaced with:

$$i_{\mathrm{FB}} = -Y_{\mathrm{FB}}\left(v_{\mathrm{B}} - e^{\mathrm{n}}_{\mathrm{FB}}\right). \tag{27}$$

The two circuits are fully equivalent when the right-hand sides of Eqs. 22 and 27 are identical as functions of v_{C} and of the noise sources, i.e., when the following two conditions are fulfilled:

$$Y_{\mathrm{FB}} = Y^0_{\mathrm{FB}}\left(1 - G\right) \tag{28}$$

$$e^{\mathrm{n}}_{\mathrm{FB}} = \frac{e^{\mathrm{n}}_{\mathrm{PA}} - e^{\mathrm{n},0}_{\mathrm{FB}}}{1 - G}. \tag{29}$$

Equation 29 means that the noise sources $e^{\mathrm{n}}_{\mathrm{FB}}$ and $e^{\mathrm{n}}_{\mathrm{PA}}$ are partly correlated.

For the equivalent circuit sketched in Fig. 18b, Eq. 26 is therefore simply replaced with:

$$v_{\mathrm{C}} = G\frac{Y_L e + \left(Y_L + Y_C\right) e^{\mathrm{n}}_{\mathrm{PA}} + i^{\mathrm{n}}_{\mathrm{PA}} - Y_{\mathrm{FB}} e^{\mathrm{n}}_{\mathrm{FB}}}{Y_L + Y_C + Y_{R\mathrm{inp}} + Y_{\mathrm{FB}}}. \tag{30}$$

Note that we have chosen to locate the equivalent admittance branch at the ideal PA input between point B and the ground (on the r.h.s. of the PA noise source) in Fig. 18b. A similar branch located between point A and the ground (on the l.h.s. of the PA noise source) would identically be equivalent to the FB loop in Fig. 18a if it were characterised by the same admittance $\widetilde{Y}_{\mathrm{FB}} = Y_{\mathrm{FB}}$ and a noise source $\widetilde{e}^{\mathrm{n}}_{\mathrm{FB}} = e^{\mathrm{n}}_{\mathrm{FB}} + v_{\mathrm{A}} - v_{\mathrm{B}}$ since v_{B} would be replaced with v_{A} in Eq. 27:

$$\widetilde{e}^{\mathrm{n}}_{\mathrm{FB}} = \frac{G e^{\mathrm{n}}_{\mathrm{PA}} - e^{\mathrm{n},0}_{\mathrm{FB}}}{1 - G}. \tag{31}$$

Since the noise sources in Eq. 26 can be considered as statistically independent, the noise factor F_{FB} with the FB loop is more conveniently derived from Eq. 26 than from Eq. 30:

$$\begin{aligned} F_{\mathrm{FB}} = 1 &+ \frac{\left|Y_L + Y_C + Y^0_{\mathrm{FB}}\right|^2\left(E^{\mathrm{n}}_{\mathrm{PA}}\right)^2 + \left(I^{\mathrm{n}}_{\mathrm{PA}}\right)^2}{\left|Y_L\right|^2\left(E^{\mathrm{n}}_{\mathrm{coil}}\right)^2} \\ &+ \frac{\left|Y^0_{\mathrm{FB}}\right|^2\left(E^{\mathrm{n},0}_{\mathrm{FB}}\right)^2}{\left|Y_L\right|^2\left(E^{\mathrm{n}}_{\mathrm{coil}}\right)^2}. \end{aligned} \tag{32}$$

However, the impact of the FB loop parameters on the Q-factor, frequency shift, and noise factor is more conveniently discussed using the scheme of Fig. 18b. When noise considerations are overlooked, the influence of the FB loop on the tank circuit resonance characteristics is solely determined by Y_{FB} which loads the tank circuit. A constant effect of the FB loop ($Y_{\mathrm{FB}} = \mathrm{const}$) is therefore achieved if the gain of the PA and the impedance in the loop are jointly varied in such a way that both sides of Eq. 28 are kept constant. At high enough gain, $|G| \gg 1$, this means that $\left|Y^0_{\mathrm{FB}}\right|$ must scale as $|G|^{-1}$, and the two contributions of the FB loop to the noise factor in Eq. 32 become negligible. More precisely, the first contribution to the noise factor arising from the enhancement of the effect of the PA voltage noise is negligible if $\left|Y_{\mathrm{FB}}^{0}\right|$ is much smaller than $\left|Y_L+Y_C\right|_{\min}$, the admittance at resonance of the stand-alone or weakly coupled tank circuit. This condition is fulfilled by more than two orders of magnitude for the internal FB of the SR560 PA (see Sec. 3.1). The second contribution, arising from the additional FB voltage noise $E_{\mathrm{FB}}^{\mathrm{n},0}$, depends on the physical origin of this noise source. For the thermal noise due to the real part of the FB impedance, $\left(E_{\mathrm{FB}}^{\mathrm{n},0}\right)^2$ scales as $\Re\left\{(Y_{\mathrm{FB}}^{0})^{-1}\right\}$ and therefore $\left|Y_{\mathrm{FB}}^{0}\right|^2\left(E_{\mathrm{FB}}^{\mathrm{n},0}\right)^2 \propto |G|^{-1}$ become negligible at high gain (still at fixed FB effect $Y_{\mathrm{FB}}=\text{const}$). Such small changes in the noise factor and in the noise-matching conditions, previously mentioned in [17], can thus be made negligible in a well-designed FB system with large enough gain. For simplicity, we neglect *both* contributions in the main text of this article, and in particular we assume a noiseless FB loop ($e_{\mathrm{FB}}^{\mathrm{n},0}=0$). For the internal FB of the SR560 PA, numerical estimates using Eq. 32 yield not only a negligible effect on the noise factor (as expected, since $Y_{\mathrm{FB}}^{0} \ll \left|Y_L+Y_C\right|_{\min}$), but also a totally negligible shift of the SNR optimum frequency.

B.2 Inductive coupling

The FB scheme with inductive coupling of Fig. 4b is modelled by the directly equivalent circuit sketched in Fig. 19a. Here, the passive input impedance R_{inp} of the PA is overlooked for simplicity, and the internal (capacitive) FB observed to exist in actual PAs (Sec. 3.1) is represented by the branch with the admittance $Y_{\mathrm{FB}}^{\mathrm{int}}$.

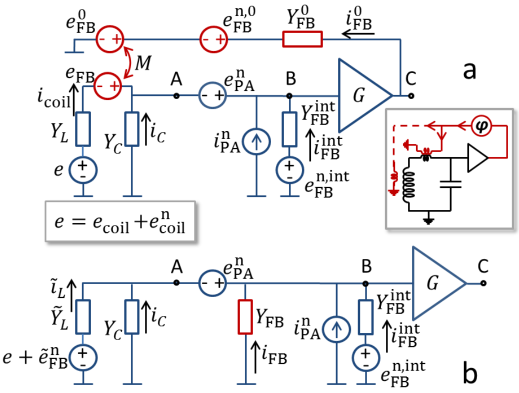

Figure 19: Two equivalent model circuits of the generalised inductive FB scheme (see the inset) introduced in Sec. 2.2.2. e_{FB} is the emf induced in the tank circuit by the FB loop through the transformer (with mutual inductance M).

The derivations are very similar to those performed for the capacitive FB scheme. Equations 20, 24, and 25 remain unchanged, Eq. 21 disappears, and additional equations are:

$$i_{\mathrm{coil}} = -Y_L\left(v_{\mathrm{A}} - e - e_{\mathrm{FB}}\right) \tag{33}$$

$$i_{\mathrm{FB}}^{\mathrm{int}} = -Y_{\mathrm{FB}}^{\mathrm{int}}\left(v_{\mathrm{B}} - e_{\mathrm{FB}}^{\mathrm{n,int}}\right) \tag{34}$$

$$i_{\mathrm{FB}}^{0} = Y_{\mathrm{FB}}^{0}\left(v_{\mathrm{C}} - e_{\mathrm{FB}}^{0} - e_{\mathrm{FB}}^{\mathrm{n},0}\right). \tag{35}$$

Equation 35 describes the actually implemented FB loop (see Fig. 11), which is not based on an ideal transconductance amplifier (which would generate an emf e_{FB} independent of the current in the tank circuit). Elimination of i_{FB}^{0} from the set of equations is obtained using:

$$e_{\mathrm{FB}} = -Z_M\, i_{\mathrm{FB}}^{0} \tag{36}$$

$$e_{\mathrm{FB}}^{0} = Z_M\, i_{\mathrm{coil}}, \tag{37}$$

where $Z_M = 2\pi f \jmath M$, and Eq. 33 becomes:

$$i_{\mathrm{coil}} = -\widetilde{Y}_L\left[\frac{v_{\mathrm{C}}}{G} - e_{\mathrm{PA}}^{\mathrm{n}} - e + Z_M Y_{\mathrm{FB}}^{0}\left(v_{\mathrm{C}} - e_{\mathrm{FB}}^{\mathrm{n},0}\right)\right], \tag{38}$$

$$\text{where } \widetilde{Y}_L = \frac{Y_L}{1 - Z_M^2 Y_L Y_{\mathrm{FB}}^{0}}. \tag{39}$$

Using the current conservation equation to eliminate i_{FB}

$$i_{\mathrm{FB}} = i_{\mathrm{coil}} + i_C + i_{\mathrm{PA}}^{\mathrm{n}}, \tag{40}$$

we derive the expression of the output voltage:

$$\begin{aligned} v_{\mathrm{C}} = {} & G\frac{\widetilde{Y}_L\left(e + Z_M Y_{\mathrm{FB}}^{0} e_{\mathrm{FB}}^{\mathrm{n},0}\right)}{\widetilde{Y}_L\left(1 + G Z_M Y_{\mathrm{FB}}^{0}\right) + Y_C + Y_{\mathrm{FB}}^{\mathrm{int}}} \\ & + G\frac{\left(\widetilde{Y}_L + Y_C\right) e_{\mathrm{PA}}^{\mathrm{n}} + i_{\mathrm{PA}}^{\mathrm{n}} + Y_{\mathrm{FB}}^{\mathrm{int}} e_{\mathrm{FB}}^{\mathrm{n,int}}}{\widetilde{Y}_L\left(1 + G Z_M Y_{\mathrm{FB}}^{0}\right) + Y_C + Y_{\mathrm{FB}}^{\mathrm{int}}}. \end{aligned} \tag{41}$$

The circuit shown in Fig. 19b describes the effect of inductive FB in terms of replacing the coil admittance Y_L with $\widetilde{Y}_L$, with an additional noise source $\tilde{e}_{\mathrm{FB}}^{\mathrm{n}}$ associated with the noise in FB loop $e_{\mathrm{FB}}^{\mathrm{n},0}$, and loading of tank circuit with a noiseless admittance Y_{FB}. The output voltage for this scheme, derived similarly to Eq. 30, is given by:

$$v_{\mathrm{C}} = G\frac{\widetilde{Y}_L(e + \tilde{e}_{\mathrm{FB}}^{\mathrm{n}}) + \left(\widetilde{Y}_L + Y_C\right) e_{\mathrm{PA}}^{\mathrm{n}} + i_{\mathrm{PA}}^{\mathrm{n}} + Y_{\mathrm{FB}}^{\mathrm{int}} e_{\mathrm{FB}}^{\mathrm{n,int}}}{\widetilde{Y}_L + Y_C + Y_{\mathrm{FB}} + Y_{\mathrm{FB}}^{\mathrm{int}}}. \tag{42}$$

Equations 41 and 42 are identical, and therefore the two circuits in Fig. 19 are equivalent, if two conditions are met:

$$Y_{\mathrm{FB}} = G Z_M Y_{\mathrm{FB}}^{0} Y_L \tag{43}$$

$$\tilde{e}_{\mathrm{FB}}^{\mathrm{n}} = Z_M Y_{\mathrm{FB}}^{0} e_{\mathrm{FB}}^{\mathrm{n},0}. \tag{44}$$

Note that the current i_{coil} actually flowing in the physical coil and responsible for radiation damping is the sum of currents in the $\widetilde{Y}_L$ and Y_{FB} branches of the circuit in Fig. 19b:

$$i_{\mathrm{coil}} = \tilde{i}_L + i_{\mathrm{FB}}. \tag{45}$$

According to Eq. 44 the additional noise in the coil can be made negligible compared to the Johnson noise of the coil in a well-designed system with a small enough Y^0_{FB}. It does not depend on the gain, whereas the FB strength can be easily varied by changing the gain (Eq. 43).

Equation 39 states that $\widetilde{Y}_L$ is the conductance of the coil in series with an additional impedance $Z_M^2 Y^0_{\mathrm{FB}}$. Note that if a perfect transconductance amplifier was used, as in Fig. 4b, the effective admittance $\widetilde{Y}_L$ would simply be replaced with Y_L in Eqs. 38, 41, and 42. This is very well approximated in our experimental implementation. The coupling transformer has low-impedance windings (≈ 5 μH each, i.e. ≈ 3 Ω at 100 kHz) compared to $1/\left|Y^0_{\mathrm{FB}}\right|$ (1 kΩ) and $1/\left|Y_L\right|$ (≈ 1.2 kΩ for 2 mH). Therefore $\left|Z_M^2 Y_L Y^0_{\mathrm{FB}}\right| \approx 3\times 10^{-6}$ in Eq. 39 and $\left|Z_M Y^0_{\mathrm{FB}}\right| \approx 3\times 10^{-3}$ in Eqs. 41, 43, and 44. As a result, the additional noise $\tilde{e}^{\mathrm{n}}_{\mathrm{FB}}$ effectively added to the Johnson noise of the coil $e^{\mathrm{n}}_{\mathrm{coil}}$ which is included in the emf e is strongly suppressed with respect to the FB loop noise $e^{\mathrm{n};0}_{\mathrm{FB}}$ (Eq. 44) and is therefore negligible, as expected for a well-designed FB system. These considerations yield the simplified equivalent models sketched in Fig. 6 in Sec. 2.2.2.

B.3 Internal feedback for a two-stage PA

We consider here an example of PA comprising two internal FB loops associated with two different amplification stages in series. They are represented in Fig. 20a with their voltage noise sources (e_1, e_2), FB admittances (Y_1^0, Y_2^0), and FB noise sources (e_1^0, e_2^0). A possible FB loop between input and output of the second stage is not considered because it does not load the tank circuit and is automatically taken in into account in the nominal gain of the PA. The current noise and input resistance of the first stage are not shown for simplicity as being undisturbed by the modification of the equivalent scheme.

Figure 20b separates out the two FB loops for clarity. The lower branch provides the output with the overall gain and PA noise:

$$G = G_1 G_2 \tag{46}$$

$$e^{\mathrm{n}}_{\mathrm{PA}} = e_1 + e_2/G_1. \tag{47}$$

Each of these FB loops can be replaced with an input admittance, as established in Sec. 2.2.1. The large FB loop is directly replaced with the branch with the admittance Y_2 and the noise source e_2^{n} connected as sketched in Fig. 20c (note that the input of the equivalent amplifier is point D, which differs from point B in Fig. 20a since the full PA noise $e^{\mathrm{n}}_{\mathrm{PA}}$ is now involved). Equations 28 and 29 directly yield

$$Y_2 = Y_2^0\left(1 - G\right) \tag{48}$$

$$e_2^{\mathrm{n}} = \left(e^{\mathrm{n}}_{\mathrm{PA}} - e_2^0\right)/\left(1 - G\right). \tag{49}$$

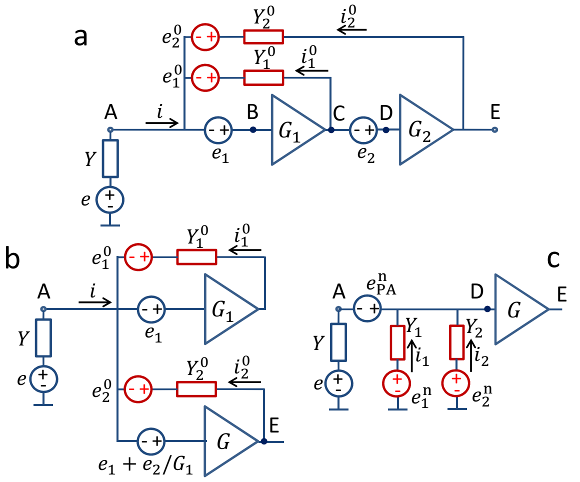

Figure 20: Simplified equivalent scheme of a 2-stage PA with two internal FB loops to its input. a: Realistic model. b: Model with separated FB loops. c: Equivalent model with equivalent input admittances and noise sources (see Fig. 18b).

The smaller FB loop could be conveniently replaced with a branch located between point A and the ground (on the l.h.s. of the PA noise source) using Eq. 31. Its noise source is then offset by $e^{\mathrm{n}}_{\mathrm{PA}}$ when the branch is shifted to point D as displayed in Fig. 20c, so that

$$Y_1 = Y_1^0\left(1 - G_1\right) \tag{50}$$

$$e_1^{\mathrm{n}} = \left(e_1 - e_1^0\right)/\left(1 - G_1\right) + e_2/G_1. \tag{51}$$

This circuit is equivalent to that of a single FB loop, with a single admittance and source term on the r.h.s. of the PA noise source (at point D, as in Fig. 18b) if the sum of currents $i_1 + i_2$ matches the current in the equivalent admittance for all values of the voltage v_{D}

$$-Y_{\mathrm{FB}}\left(v_{\mathrm{D}} - e^{\mathrm{n}}_{\mathrm{FB}}\right) = -Y_1\left(v_{\mathrm{D}} - e_1^{\mathrm{n}}\right) - Y_2\left(v_{\mathrm{D}} - e_2^{\mathrm{n}}\right). \tag{52}$$

This yields the equivalent admittance and noise terms:

$$Y_{\mathrm{FB}} = Y_1 + Y_2 \tag{53}$$

$$e^{\mathrm{n}}_{\mathrm{FB}} = \left[Y_1 e_1^{\mathrm{n}} + Y_2 e_2^{\mathrm{n}}\right]/Y_{\mathrm{FB}} \tag{54}$$

The general expression of the equivalent noise term (Eq. 54) has a simpler form for noiseless FB elements (such as capacitors, a plausible assumption for internal FB), i.e. for negligible e_1^0 and e_2^0

$$\left(Y_1 + Y_2\right)e^{\mathrm{n}}_{\mathrm{FB}} = Y_1\left[\frac{e_1}{1 - G_1} + \frac{e_2}{G_1}\right] + Y_2\frac{e_1 + e_2/G_1}{1 - G} \tag{55}$$

$$\approx -\left(Y_1 + \frac{Y_2}{G_2}\right)\frac{e_1}{G_1} + \left(Y_1 - \frac{Y_2}{G}\right)\frac{e_2}{G_1}, \tag{56}$$

where Eq. 56 is a high-gain approximation ($G_1 \gg 1$).

Therefore the scheme of Fig. 18b with the parameters computed in Eqs. 46, 47, 53, and 54 describes a PA with two internal FB loops located between each output stage and the input of the PA. As is the case for a simple PA, if the gain is high enough ($G_1 \gg 1, G \gg 1$) the additional noise source term can be neglected and the final effect of the internal FB of the PA is a mere change in the input impedance without SNR degradation. One could easily extend such consideration to any numbers of FB loops in a PA.

B.4 Internal FB for a differential PA

We finally consider a differential PA in which internal FB can be due to capacitive coupling in each of the identical input stages (Fig. 21a) or between the output and each input (Fig. 21b). The simple models in Fig. 21 assume negligible noise sources and consider possibly different FB admittances Y_0^+ and Y_0^-. The PU coil and main tuning capacitor are fully floating, but admittances Y_A and Y_B resulting for instance from the capacitances of the connecting cables and PA inputs, separately connect the PA inputs to the ground. The currents are expressed as functions of voltage values at points A to F:

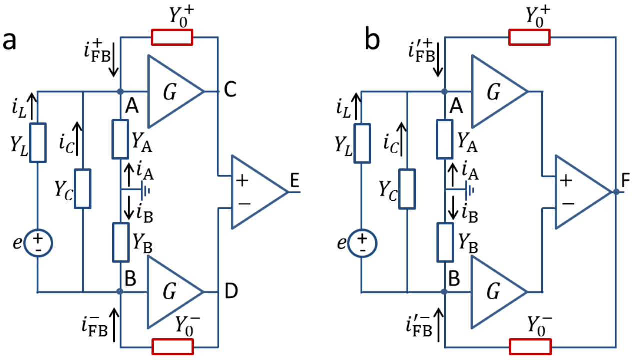

Figure 21: Simplified models of a differential PA with internal FB loops to its inputs. a: short FB loops in each input stage. b: Long FB loops from the difference output.

$$
\begin{aligned}
i_L &= -Y_L\left(v_\mathrm{A} - v_\mathrm{B} - e\right) && (57)\\
i_C &= -Y_C\left(v_\mathrm{A} - v_\mathrm{B}\right) && (58)\\
i_\mathrm{A} &= -Y_\mathrm{A} v_\mathrm{A} \text{ and } i_\mathrm{B} = -Y_\mathrm{B} v_\mathrm{B} && (59)\\
i_\mathrm{FB}^+ &= Y_0^+\left(v_\mathrm{C} - v_\mathrm{A}\right) \text{ and } i_\mathrm{FB}^- = Y_0^-\left(v_\mathrm{D} - v_\mathrm{B}\right) && (60)\\
i'^{+}_\mathrm{FB} &= Y_0^+\left(v_\mathrm{F} - v_\mathrm{A}\right) \text{ and } i'^{-}_\mathrm{FB} = Y_0^-\left(v_\mathrm{F} - v_\mathrm{B}\right)\ . && (61)
\end{aligned}
$$

For the short FB loops assumed in Fig. 21a the null sums of currents at points A and B are written:

$$
\begin{aligned}
i_L + i_C + i_\mathrm{A} + i_\mathrm{FB}^+ &= 0 && (62)\\
-i_L - i_C + i_\mathrm{B} + i_\mathrm{FB}^- &= 0, && (63)
\end{aligned}
$$

and two relations between v_A, v_B, and e are deduced from Eq. 62 and 63, respectively:

$$
\begin{aligned}
a v_\mathrm{A} + b v_\mathrm{B} &= -Y_L e && (64)\\
c v_\mathrm{A} + d v_\mathrm{B} &= Y_L e, && (65)
\end{aligned}
$$

where

$$
\begin{aligned}
a &= -\left(Y_C + Y_L\right) - \tilde{a} \text{ with } \tilde{a} = (1-G)\, Y_0^+ + Y_\mathrm{A} && (66)\\
b &= c = Y_C + Y_L && (67)\\
d &= -\left(Y_C + Y_L\right) - \tilde{d} \text{ with } \tilde{d} = (1-G)\, Y_0^- + Y_\mathrm{B}. && (68)
\end{aligned}
$$

The solutions of Eqs. 64 and 65 are

$$
v_\mathrm{A} = \frac{-eY_L\,(d+b)}{ad-bc} \text{ and } v_\mathrm{B} = \frac{eY_L\,(c+a)}{ad-bc}, \qquad (69)
$$

therefore

$$
\begin{aligned}
v_\mathrm{A} - v_\mathrm{B} &= \frac{eY_L}{Y_C + Y_L + \tilde{Y}} && (70)\\
\text{with } \tilde{Y} &= \tilde{a}\tilde{d}/\left(\tilde{a} + \tilde{d}\right). && (71)
\end{aligned}
$$

Noting

$$
\begin{aligned}
Y_0 &= \left(Y_0^+ + Y_0^-\right)/2 \text{ and } \delta Y_0 = \left(Y_0^+ - Y_0^-\right)/2 && (72)\\
Y_\mathrm{AB} &= \left(Y_\mathrm{A} + Y_\mathrm{B}\right)/2 \text{ and } \delta Y_\mathrm{AB} = \left(Y_\mathrm{A} - Y_\mathrm{B}\right)/2, && (73)
\end{aligned}
$$

the added admittance $\tilde{Y}$ in the denominator of Eq. 70 can be written

$$
\tilde{Y} = \frac{(1-G)\,Y_0 + Y_\mathrm{AB}}{2}\left[1 - \left(\frac{(1-G)\,\delta Y_0 + \delta Y_\mathrm{AB}}{(1-G)\,Y_0 + Y_\mathrm{AB}}\right)^2\right]. \qquad (74)
$$

For a balanced setup ($\delta Y_0 = \delta Y_{AB} = 0$) the resonance is shifted due to the added capacitance ($Y_{AB}/2$) and modified by the FB term $(1-G)\,Y_0/2$: the output voltage is

$$
v_\mathrm{E} = G\left(v_\mathrm{A} - v_\mathrm{B}\right) = \frac{eGY_L}{Y_C + Y_L + Y_\mathrm{AB}/2 + Y_0\,(1-G)\,/2}. \qquad (75)
$$

Interestingly, imbalance can reduce $\left|\tilde{Y}\right|$ and therefore the strength of the influence of internal FB on the resonance. It is in particular cancelled if $Y_\mathrm{A} = Y_0^+(G-1)$ or $Y_\mathrm{B} = Y_0^-(G-1)$ ($\tilde{a} = 0$ or $\tilde{d} = 0$ in Eq. B5-16 yields $\tilde{Y} = 0$).

For the long FB loops assumed in Fig. 21b the null sums of currents at points A and B are :

$$
\begin{aligned}
i_L + i_C + i_\mathrm{A} + i'^{+}_\mathrm{FB} &= 0 && (76)\\
-i_L - i_C + i_\mathrm{B} + i'^{-}_\mathrm{FB} &= 0, && (77)
\end{aligned}
$$

and the two relations between v_A, v_B, and e deduced from Eq. 76 and 77 are:

$$
\begin{aligned}
a' v_\mathrm{A} + b' v_\mathrm{B} &= -Y_L e && (78)\\
c' v_\mathrm{A} + d' v_\mathrm{B} &= Y_L e, && (79)
\end{aligned}
$$

where

$$
\begin{aligned}
a' &= -\left(Y_C + Y_L\right) - \tilde{a}' \text{ with } \tilde{a}' = (1-G)\, Y_0^+ + Y_\mathrm{A} && (80)\\
b' &= Y_C + Y_L - GY_0^+ && (81)\\
c' &= Y_C + Y_L + GY_0^- && (82)\\
d' &= -\left(Y_C + Y_L\right) - \tilde{d}' \text{ with } \tilde{d}' = (1+G)\, Y_0^- + Y_\mathrm{B} && (83)
\end{aligned}
$$

The coefficients a and a' defined by Eqs. 66 and 80 are identical, but the remaining coefficients in Eqs. 78 and 79 are different. The solutions, formally similar to Eq. 69, are

$$v_{\mathrm{A}} = \frac{-eY_L\left(d'+b'\right)}{a'd'-b'c'} \text{ and } v_{\mathrm{B}} = \frac{eY_L\left(c'+a'\right)}{a'd'-b'c'}. \tag{84}$$

To compute $v_A - v_B$, we use

$$-a'-c'-b'-d' = \tilde{a}'+\tilde{d}'+G\left(Y_0^+ - Y_0^-\right) \tag{85}$$

$$\begin{aligned} a'd'-b'c' &= \left(Y_C+Y_L\right)\left(\tilde{a}'+\tilde{d}'\right)+\tilde{a}'\tilde{d}' \\ &\quad + \left(Y_C+Y_L\right)G\left(Y_0^+ - Y_0^-\right)+G^2Y_0^+Y_0^- \end{aligned} \tag{86}$$

therefore

$$v_{\mathrm{A}} - v_{\mathrm{B}} = \frac{eY_L}{Y_C+Y_L+\tilde{Y}'} \tag{87}$$

$$\text{with } \tilde{Y}' = \frac{\tilde{a}'\tilde{d}'+G^2Y_0^+Y_0^-}{\tilde{a}'+\tilde{d}'+G\left(Y_0^+ - Y_0^-\right)} \tag{88}$$

$$= \frac{Y_0+Y_{\mathrm{AB}}}{2} + \frac{G\left(Y_0\delta Y_{\mathrm{AB}} - Y_{\mathrm{AB}}\delta Y_0\right) - \left(\delta Y_{\mathrm{AB}}+\delta Y_0\right)^2/2}{Y_{\mathrm{AB}}+Y_0} \tag{89}$$

When the FB admittances are equal ($\delta Y_0 = 0$), the added admittance $\tilde{Y}'$ of Eq. 89 in the denominator of Eq. 87 is

$$\tilde{Y}' = \frac{Y_0+Y_{\mathrm{AB}}}{2} + \frac{G\delta Y_{\mathrm{AB}} - \delta Y_{\mathrm{AB}}^2/2Y_0}{1+Y_{\mathrm{AB}}/Y_0}. \tag{90}$$

Conversely, when the input admittances are equal ($\delta Y_{\mathrm{AB}} = 0$), the added admittance $\tilde{Y}'$ is

$$\tilde{Y}' = \frac{Y_0+Y_{\mathrm{AB}}}{2} - \frac{GY_{\mathrm{AB}}\delta Y_0 + \delta Y_0^2/2}{Y_0+Y_{\mathrm{AB}}}. \tag{91}$$

Equation 89 shows that when the setup is fully balanced, with $\delta Y_{\mathrm{AB}} = 0$ and $\delta Y_0 = 0$, $\tilde{Y}'$ reduces to its first terms $\left(Y_0+Y_{\mathrm{AB}}\right)/2$. For the same values Y_0 of internal couplings, FB from the difference output is gain-independent and highly suppressed compared to the situation of independent FB loops (Eq. 74): the tank circuit is loaded by an equivalent admittance $Y_0/2$ instead of $Y_0\left(G-1\right)/2$. If, however, an imbalance exists in the connections to the ground of the differential inputs ($\delta Y_{\mathrm{AB}} \neq 0$), a contribution linear in G and δY_{AB} appears in $\tilde{Y}'$ (Eq. 91). The benefit of the suppression of the internal FB by differential operation is reduced, and the PU coil resonance can be strongly affected at high gain.

Series of measurements of PU coil resonances have been performed with the SR560 PA for $G = \pm 10$, ± 100, ± 500, and ± 1000 for balanced cable lengths (1-m-long, $C_{1\mathrm{m}} = 100$ pF) or with an additional 0.35, 0.5 m or 1 m length of cable on either input. Noting

$$Y_{1\mathrm{m}} = 2\pi\jmath f_0' C_{1\mathrm{m}} \;\left(\left|Y_{1\mathrm{m}}\right| = 54.95\ \mu\mathrm{S} \text{ at } 87.45\ \mathrm{kHz}\right) \tag{92}$$

and assuming that the input capacitance of each PA channel is 25 pF (as specified for the SR560), recordings have thus been performed for:

$$Y_{\mathrm{AB}} = 5Y_{1\mathrm{m}}/4\ ,\ \delta Y_{\mathrm{AB}} = 0 \tag{93}$$

$$Y_{\mathrm{AB}} = 2.85Y_{1\mathrm{m}}/2\ ,\ \delta Y_{\mathrm{AB}} = \pm 0.35Y_{1\mathrm{m}} \tag{94}$$

$$Y_{\mathrm{AB}} = 3Y_{1\mathrm{m}}/2\ ,\ \delta Y_{\mathrm{AB}} = \pm 0.5Y_{1\mathrm{m}} \tag{95}$$

$$Y_{\mathrm{AB}} = 7Y_{1\mathrm{m}}/4\ ,\ \delta Y_{\mathrm{AB}} = \pm Y_{1\mathrm{m}} \tag{96}$$

and differences for $\tilde{Y}'$ in Eq. 89 when the lengths of uneven cables are swapped are simply

$$\Delta\tilde{Y}' = \frac{\left(2GY_0 - 2\delta Y_0\right)\delta Y_{\mathrm{AB}}}{Y_{\mathrm{AB}}+Y_0} \approx \frac{2GY_0\delta Y_{\mathrm{AB}}}{Y_{\mathrm{AB}}+Y_0}, \tag{97}$$

which can be deduced from resonance data (R_{eff}^{-1} and and $f_0' - f_0$, see Eqs. 15 and 16) for each gain value:

$$\Re\left[\Delta\tilde{Y}'\right] = \Delta R_{\mathrm{eff}}^{-1} \tag{98}$$

$$\Im\left[\Delta\tilde{Y}'\right] = \Delta\left(f_0' - f_0\right)/\left(\pi f_o'^2 L\right) \tag{99}$$

Equation 97 can be used to deduce Y_0 from resonance data through $\Delta\tilde{Y}'$

$$Y_0 = \frac{Y_{\mathrm{AB}}\Delta\tilde{Y}'/G}{2\delta Y_{\mathrm{AB}} - \Delta\tilde{Y}'/G} \approx \frac{Y_{\mathrm{AB}}}{2\delta Y_{\mathrm{AB}}}\Delta\tilde{Y}'/G \tag{100}$$

since $\left|\Delta\tilde{Y}'/G\right|$ experimentally lies well below 0.1 μS and is negligible in the denominator of the exact r.h.s in Eq. 100. Therefore Y_0 is directly proportional to $\Delta\tilde{Y}'/G$ with well-defined coefficients depending on cable lengths. Figure 22 displays selected results corresponding to measurements performed on a tuned PU coil (see Sec. 3.1). Most results obtained at low gain ($G = 10$) exceed the displayed range, but the high-gain data yield fairly consistent values for the average internal FB admittance Y_0, which supports the soundness of the simple model in Fig. 21b. Moreover, theses values also correspond to estimates derived in Sec. 3.1 when the same PA was used in single-ended configuration.

References

[1] D. I. Hoult, R. E. Richards, Signal-to-noise ratio of nuclear magnetic-resonance experiment, J. Magn. Reson. 24 (1) (1976) 71–85 (1976).

[2] W. Dominguez-Viqueira, W. Berger, J. Parra-Robles, G. E. Santyr, Litz Wire Radiofrequency Receive Coils for Hyperpolarized Noble Gas MR Imaging of Rodent Lungs at 73.5 mT, Concepts Magn. Reso. B. 37B (2) (2010) 75–85 (2010).

[3] D. G. Gadian, F. N. H. Robinson, Radiofrequency Losses in NMR Experiments on Electrically Conducting Samples, J. Magn. Reson. 34 (2) (1979) 449–455 (1979).

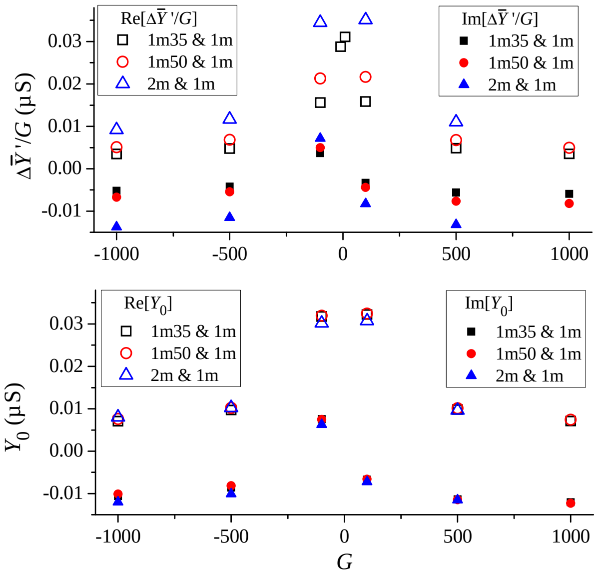

Figure 22: Processed resonance data obtained with unequal cable lengths (see legends). Top panel: Real and imaginary parts of differences $\Delta\tilde{Y}'$ of the added admittances when uneven cables are swapped (Eq. 97). Bottom panel: values of the average internal FB admittance Y_0 inferred from the data in Fig. 22a using Eq. 100.

[4] T. W. Redpath, J. M. S. Hutchison, Estimating Patient Dielectric Losses in NMR Imagers, Magn. Reson. Imaging 2 (4) (1984) 295–300 (1984).

[5] M. Hayden, C. Bidinosti, E. Chapple, Specific absorption rates and signal-to-noise ratio limitations for MRI in very-low magnetic fields, Concepts Magn. Reso. A 40A (6) (2012) 281–294 (2012). `doi:10.1002/cmr.a.21247`.

[6] D. I. Hoult, P. C. Lauterbur, Sensitivity of the Zeugmatographic Experiment Involving Human Samples, J. Magn. Reson. 34 (2) (1979) 425–433 (1979).

[7] L. Darrasse, J. Ginefri, Perspectives with cryogenic RF probes in biomedical MRI, Biochimie 85 (9) (2003) 915–937 (2003). `doi:10.1016/j.biochi.2003.09.016`.

[8] A. Abragam, The Principles of Nuclear Magnetism, Clarendon Press, 1961 (1961).

[9] P. Broekaert, J. Jeener, Suppression of Radiation Damping in NMR in Liquids by Active Electronic Feedback, J. Magn. Reson., Ser. A 113 (1) (1995) 60–64 (1995).

[10] M. Gueron, A Coupled Resonator Model of the Detection of Nuclear-Magnetic-Resonance - Radiation Damping, Frequency Pushing, Spin Noise, and the Signal-to-Noise Ratio, Magnet. Reson. Med. 19 (1) (1991) 31–41 (1991).

[11] D. Kleppner, N. F. Ramsey, H. M. Goldenberg, Theory of Hydrogen Maser, Phys. Rev. 126 (2) (1962) 603–615 (1962).

[12] D. I. Hoult, G. Kolansky, D. Kripiakevich, S. B. King, The NMR multi-transmit phased array: a Cartesian feedback approach, J. Magn. Reson. 171 (1) (2004) 64–70 (2004).

[13] P. B. Roemer, W. A. Edelstein, C. E. Hayes, S. P. Souza, O. M. Mueller, The NMR Phased-Array, Magnet. Reson. Med. 16 (2) (1990) 192–225 (1990).

[14] H. Gilles, Y. Monfort, J. Hamel, 3He MASER for Earth magnetic field measurement, Rev. Sci. Instrum. 74 (10) (2003) 4515–4520 (2003).

[15] R. Chidambaram, A Method of Reducing Radiation Damping in Nuclear Magnetic Resonance, Nuovo Cimento 13 (2) (1959) 405–409 (1959).

[16] A. Szoke, S. Meiboom, Radiation Damping in Nuclear Magnetic Resonance, Phys. Rev. 113 (2) (1959) 585–586 (1959).

[17] D. I. Hoult, Fast Recovery, High Sensitivity NMR Probe and Pre-Amplifier for Low-Frequencies, Rev. Sci. Instrum. 50 (2) (1979) 193–200 (1979).

[18] E. Baudin, K. Safiullin, S. W. Morgan, P. J. Nacher, An active feedback scheme for low field NMR experiments, J. Phys. Conf. Ser. 294 (1) (2011) 012009 (2011).

[19] A. Louis Joseph, D. Abergel, J. Y. Lallemand, Neutralization of Radiation Damping by Selective Feedback on a 400-MHz NMR Spectrometer, J. Biomol. NMR 5 (2) (1995) 212–216 (1995).

[20] M. T. Poeschko, J. Schlagnitweit, G. Huber, M. Nausner, M. Hornicakova, H. Desvaux, N. Mueller, On the Tuning of High-Resolution NMR Probes, Chemphyschem 15 (16) (2014) 3639–3645 (2014).

[21] D. I. Hoult, NMR Receiver - Description and Analysis of Design, Prog. Nucl. Mag. Res. Sp. 12 (1978) 41–77 (1978).

[22] A. M. Coffey, M. L. Truong, E. Y. Chekmenev, Low-field MRI can be more sensitive than high-field MRI, J. Magn. Reson. 237 (2013) 169–174 (2013).

[23] C. R. Sullivan, Optimal choice for number of strands in a litz-wire transformer winding, IEEE T. Power Electr. 14 (2) (1999) 283–291 (1999).

[24] X. Nan, C. R. Sullivan, An Equivalent Complex Permeability Model for Litz-Wire Windings, Ieee T. Ind. Appl. 45 (2) (2009) 854–860 (2009). `doi:10.1109/tia.2009.2013594`.

[25] R. P. Wojda, M. K. Kazimierczuk, Winding resistance of litz-wire and multi-strand inductors, IET Power Electron. 5 (2) (2012) 257–268 (2012). `doi:10.1049/iet-pel.2010.0359`.

[26] C. Motchenbacher, J. Connelly, Low noise electronic system design, Chapters 5 and 6, J. Wiley & Sons, 1993 (1993).

[27] D. I. Hoult, Receiver design for MR, eMagRes (2011) 1–21 (2011).

[28] W. M. Leach, Fundamentals of Low-Noise Analog Circuit-Design, P. Ieee 82 (10) (1994) 1515–1538 (1994).

[29] E. Fukushima, Experimental Pulse NMR: A Nuts and Bolts Approach, CRC Press, 1993 (1993).

[30] S. Mandal, S. Utsuzawa, D. G. Cory, M. Huerlimann, M. Poitzsch, Y. Q. Song, An ultra-broadband low-frequency magnetic resonance system, J. Magn. Reson. 242 (2014) 113–125 (2014).

[31] E. Bendet-Taicher, N. Mueller, A. Jerschow, Dependence of NMR Noise Line Shapes on Tuning, Matching, and Transmission Line Properties, Concepts Magn. Reso. B. 44 (1) (2014) 1–11 (2014).

[32] D. I. Hoult, G. Kolansky, D. Kripiakevich, A 'hi-fi' Cartesian feedback spectrometer for precise quantitation and superior performance, J. Magn. Reson. 171 (1) (2004) 57–63 (2004).

[33] P. R. Gray, P. J. Hurst, S. H. Lewis, R. G. Meyer, Analysis and Design of Analog Integrated Circuits, 5th Edition, Wiley, 2009 (2009).

[34] J. Jeener, Collective Effects in Liquid NMR: Dipolar Field and Radiation Damping, in: D. M. Grant, R. K. Harris (Eds.), Advances in NMR, Vol. 9 of Encyclopedia of Nuclear Magnetic Resonance, John Wiley & Sons, Ltd, Chichester, 2002, pp. 642–679 (2002).

[35] M. E. Hayden, E. Baudin, G. Tastevin, P. J. Nacher, NMR Time Reversal as a Probe of Incipient Turbulent Spin Dynamics, Phys. Rev. Lett. 99 (13) (2007) 137602 (2007).

[36] S. W. Morgan, E. Baudin, G. Huber, P. Berthault, G. Tastevin, M. Goldman, P.-J. Nacher, H. Desvaux, Multiple echoes due to distant dipolar fields in NMR of hyperpolarized noble gas solutions, Eur. Phys. J. D 67 (2013) 29 (2013). `doi:{10.1140/epjd/e2012-30470-0}`.

[37] H. Desvaux, Non-linear liquid-state NMR, Prog. Nucl. Mag. Res. Sp. 70 (2013) 50–71 (2013).

[38] D. J. Y. Marion, G. Huber, P. Berthault, H. Desvaux, Observation of noise-triggered chaotic emissions in an NMR-maser, Chemphyschem 9 (10) (2008) 1395–1401 (2008).

[39] K. Safiullin, C. Talbot, P.-J. Nacher, Achieving high spatial resolution and high SNR in low-field MRI of hyperpolarised gases with Slow Low Angle SHot, J. Magn. Reson. 227 (2013) 72–86 (2013).

[40] P.-J. Nacher, G. Tastevin, C. Bidinosti, Exploration of TRASE MRI at Low Magnetic Field: Potential Performance and Limitations, in: Proc. 14 th Euromar, 2018, p. P338 (2018).

[41] C. P. Bidinosti, J. Choukeife, P.-J. Nacher, G. Tastevin, In vivo NMR of hyperpolarized 3He in the human lung at very low magnetic fields, J. Magn. Reson. 162 (1) (2003) 122 – 132 (2003).

[42] I. C. Ruset, L. L. Tsai, R. W. Mair, S. Patz, M. I. Hrovat, M. S. Rosen, I. Muradian, J. Ng, G. P. Topulos, J. P. Butler, R. L. Walsworth, F. W. Hersman, A system for open-access He-3 human lung imaging at very low field, Concepts Magn. Reson. B 29B (4) (2006) 210–221 (2006).

[43] K. P. Pruessmann, M. Weiger, M. B. Scheidegger, P. Boesiger, SENSE: Sensitivity encoding for fast MRI, Magnet. Reson. Med. 42 (5) (1999) 952–962 (1999).